

AD-A255 447



2

PSU LEPS/92-08

FINAL TECHNICAL REPORT

AFOSR GRANT 91-0302
June 15, 1991-June 14, 1992
Gerald A. Smith
July 30, 1992

DTIC
ELECTED
SEP 14 1992
S A 0

This document has been approved
for public release and sale; its
distribution is unlimited.

FINAL 15 Jun 91 TO 14 Jun 92

Excitation of Nuclei by Antiproton Annihilation
at rest

2301/B2

Dr Gerald Smith

Penn State Univ
Dept of Physics
303 Osmond Laboratory
University Park, PA 16802

AFOSR/NE
Bldg 410
Bolling AFB Washington DC 20332-6448
Dr. Ralph Kelley

AFOSR-91-0302

APPROVED FOR PUBLIC RELEASE: DISTRIBUTION IS UNLIMITED

Research leading to the detailed characterization of antiproton annihilation in nuclei has resulted in three publications during the past year. We have reported on neutron yields and angular distributions from annihilation in uranium. This work is important to our SHIVA Star subcritical microfission measurements currently in progress at the Phillips Laboratory, Kirtland AFB. Proton spectra indicate the presence of multinucleon annihilation in carbon and uranium targets. This is important in determining the pre-fission yield of nucleons in annihilation on uranium. The existence of rare hypernuclei formed in antiproton annihilation on uranium and bismuth has been observed. These states live a fraction of a nanosecond, and are of considerable interest to theorists trying to understand the binding of particles in heavy nuclei.

82

4 1 1 1 1

92-25089



278869

66P8

UNCLASSIFIED

UNCLASSIFIED

UNCLASSIFIED

UNLIMITED

Date: July 30, 1992

To: Dr. Ralph Kelley (AFOSR)

From: Gerald A. Smith, Principal Investigator, AFOSR 91-0302

Re: Final Technical Report, June 15, 1991-June 14, 1992

SUMMARY

Research leading to the detailed characterization of antiproton annihilation in nuclei has resulted in three publications during the past year. We have reported on neutron yields and angular distributions from annihilation in uranium. This work is important to our SHIVA Star subcritical microfission measurements currently in progress at the Phillips Laboratory, Kirtland AFB. Proton spectra indicate the presence of multinucleon annihilation in carbon and uranium targets. This is important in determining the pre-fission yield of nucleons in annihilation on uranium. The existence of rare hypernuclei formed in antiproton annihilation on uranium and bismuth has been observed. These states live a fraction of a nanosecond, and are of considerable interest to theorists trying to understand the binding of particles in heavy nuclei.

RESEARCH OBJECTIVES

The objective of this research is to accurately characterize the yields and energy spectra of charged and neutral elementary particles emitted from antiproton annihilation at rest in nuclei (carbon, bismuth and uranium). The particles include gamma-rays, pions, kaons, protons, neutrons, light nuclear fragments and fission fragments. This information is being used to test concepts which may be used in the design of antimatter propulsion systems, as well as other applications such as intense neutron sources and pumped nuclear lasers.

RESULTS OF RESEARCH

In a previous final technical report, AFOSR grant 87-0246, May 1, 1987-April 30, 1991, we described results from research on antiproton-induced fission in uranium targets. Neutron and gamma-ray spectra demonstrated very hot fission fragment formation, as well as intense initial heating of the nucleus before fission due to the intranuclear cascade. Our group was the first to observe neutrons and gamma-rays from antiproton-induced fission. Charged pion and neutral high energy gamma-ray spectra show that approximately 450 MeV of energy is transferred to the nucleus by the annihilation, resulting in the ejection of neutrons and protons and the subsequent fission.

In the last year we have concentrated our efforts in three areas. First, we have completed a final characterization of antiproton-induced fis-

sion in uranium, including fitted yields of neutrons from the intranuclear cascade and fission as well as angular distributions of fission neutrons which provide a measurement of the temperature of excited fission fragments. This temperature is approximately 50 MeV per fragment, a factor of 2.5 larger than conventional fission experiments with low energy neutrons. These results are of paramount importance to our current program of studying subcritical micro-fission at the Phillips Laboratory, Kirtland AFB, and have been recently published in Physical Review C (1, Appendix I). New studies of similar effects in bismuth targets is presently in progress. Graduate student Bin Chen has made major contributions to this work.

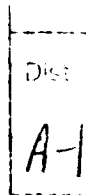
Second, a new study of fast proton emission from antiproton annihilation in carbon and uranium indicates that collective phenomena in the annihilation are important. We find that typically 20% of the annihilations take place on two nucleons, rather than on one nucleon as conventional wisdom suggests. This is a quantum-mechanical phenomenon, and is manifest by the presence of high energy protons seen beyond the kinematic boundary allowed by single nucleon annihilation. These results have been published in Z. Phys. A (2, Appendix II) and are largely the result of efforts by Dr. E. Minor, who was supported under our previous AFOSR grant as a graduate student. A similar study of fast deuteron emission is in progress. This work is a collaborative effort with Alexander Sibirtsev of the Institute of Theoretical and Experiment Physics, Moscow. A summer NSF sponsored student, Cassandra Lam of the State University of New York, Binghamton, is also participating.

Third, we have completed a study of hypernuclear formation in antiproton-annihilation in heavy nuclei. The existence of hypernuclear states (where a Λ hyperon binds to a nucleus in place of a neutron) in bismuth and uranium has been confirmed, and lifetimes in the range of a few times 10^{-10} seconds have been measured. This extremely novel work permits new theoretical investigations of the binding of particles in heavy nuclei. Results have been recently submitted to Phys. Rev. C (3, Appendix III).

PUBLICATIONS

- (1) Neutron Yields and Angular Distributions Produced in Antiproton Annihilation at Rest in Uranium, B. Chen, T.A. Armstrong, R.A. Lewis, R. Newton, G.A. Smith, J.P. Bocquet, F. Malek, H. Nifenecker, M. Maurel, E. Monnand, P. Perrin, C. Ristori, G. Ericsson, T. Johansson, G. Tibell, M. Rey-Campagnolle, S. Polikanov, T. Krogulski and J. Mougey, Phys. Rev. C, 45, 2332 (1992).
- (2) Multinucleon Phenomena and Proton Spectra Characterizing Antiproton Annihilation at Rest in Nuclei, E.D. Minor, T.A. Armstrong, B. Chen, R.A. Lewis and G.A. Smith, Z. Phys. A, 342, 447 (1992).
- (3) Fission of Heavy Hypernuclei Formed in Antiproton Annihilation, T.A. Armstrong, J.P. Bocquet, G. Ericsson, T. Johansson, T. Krogulski, R.A. Lewis, F. Malek, M. Maurel, E. Monnand, J. Mougey, H. Nifenecker, J. Passaneau, P. Perrin, S.M. Polikanov, M. Rey-Campagnolle, C. Ristori, G.A. Smith and G. Tibell, submitted to Phys. Rev. C (1992).

DTIC QUALITY INSPECTED 3



PARTICIPATING PROFESSIONALS

R.A. Lewis, Ph.D. 1966, "Pion Photoproduction Angular Distributions"

G.A. Smith, Ph.D. 1961, "Proton-Proton Interactions at 2.85 BeV"

COUPLING ACTIVITIES

a) Colloquia, Lectures and Seminars

1. Invited papers, Workshop on Nucleon-Antinucleon Interactions, ITEP, Moscow, USSR, 1991.
2. Seminar, Advanced Concepts Seminar, T-Division, Los Alamos National Laboratory, Los Alamos, New Mexico, 1991.
3. Invited paper, International Conference on Emerging Nuclear Systems, Monterey, California, 1991.
4. Invited paper, Conference on Advanced SEI Technologies, Cleveland, Ohio, 1991.
5. Invited paper, NASA Symposium on Advance Propulsion Concepts, Jet Propulsion Laboratory, Pasadena, California, 1992.
6. Seminar, Nuclear Weapons Technology Forum, Los Alamos National Laboratory, Los Alamos, NM, 1992.
7. Seminar, Air Force Institute of Technology, Wright-Patterson AFB, Dayton, OH, 1992.
8. Seminar, Aeronautical and Astronautical Engineering Dept., Ohio State University, Columbus, OH, 1992.

b) Consulting

Los Alamos National Laboratory, consultant contract, Oct. 1, 1991-Sept. 30, 1992, contact - Dr. Johndale Solem (T-Div.), Dr. Nicholas King (P-15 Div.).

Phillips Laboratory, Kirtland AFB, IPA contract, Oct. 1, 1991-Sept. 30, 1992, contact - Dr. James Degnan (High Energy Plasma Div.).

Neutron yields and angular distributions produced in antiproton annihilation at rest in uranium

B. Chen, T. A. Armstrong, R. A. Lewis, R. Newton, and G. A. Smith

Laboratory for Elementary Particle Science, Department of Physics, The Pennsylvania State University, University Park, Pennsylvania 16802

J. P. Bocquet and F. Malek

Institut des Sciences Nucléaires de Grenoble, 53 Avenue des Martyrs, 38026 Grenoble CEDEX, France

H. Nifenecker

*Institut des Sciences Nucléaires de Grenoble CEDEX, 53 Avenue des Martyrs, 38026 Grenoble CEDEX, France
and DRFMC/LIH Centre d'Etudes Nucléaires de Grenoble, Boîte Postale 85X, 38041 Grenoble CEDEX, France*

M. Maurel, E. Monnand, P. Perrin, and C. Ristori

DRFMC, Centre d'Etudes Nucléaires de Grenoble, Boîte Postale 85X, 38041 Grenoble CEDEX, France

G. Ericsson, T. Johansson, and G. Tibell

Department of Radiation Sciences, P.O. Box 535, S-75121 Uppsala, Sweden

M. Rey-Campagnolle

*Centre de Spectrométrie Nucléaire et de Spectrométrie de Masse, Institut National de Physique Nucléaire et de Physique des Particules,
Centre National de la Recherche Scientifique F-91405 Orsay, France
and CERN/PPE, CH-1211 Geneva 23, Switzerland*

S. Polikanov

Gesellschaft für Schwerionenforschung Darmstadt, Postfach 110541, D-6100 Darmstadt, Germany

T. Krogulski

Warsaw University, Bialystok Branch, PL-15-424 Bialystok, Poland

J. Mougey

*Continuous Electron Beam Accelerator Facility, Newport News, Virginia 23606**(Received 18 December 1991)*

Measurements of neutron yields and their angular distributions in coincidence with fission fragments produced in antiproton annihilation at rest in a natural uranium target have been carried out Low Energy Antiproton Ring (LEAR) at CERN. A total of 16.3 ± 0.9 neutrons per annihilation have been found, distributed among direct knockout (27%), evaporation (21%), and fission (52%) processes. Angular distributions show that neutrons below approximately 5 MeV result entirely from moving fission fragments, and above approximately 12 MeV entirely from the excited, precession nucleus. An estimate of the angular momentum of the excited fission fragment gives $\sim 13\hbar$. We are able to account for all baryons produced in annihilation, including neutrons from this experiment and light charged nuclei found in another LEAR experiment, to within 4.5 ± 2.5 of the initial 237 units in the initial state.

PACS number(s): 25.43.+t

I. INTRODUCTION

When an antiproton stops in uranium, it forms an antiprotonic atom which cascades down to the $n = 11$, $l = 10$ atomic level before annihilating [1]. The annihilation occurs on the nuclear surface, creating approximately five high-momentum pions. Typically, 30% of the pions pass through greater than one mean free path of nuclear matter, initiating an intranuclear cascade (INC). The nuclear excitation is different from that induced by particle beams in that the primary particles are born on the nuclear surface. From measurements of interactions with neutrons [2], pions [3,4], gamma rays [5], and pro-

tons [6], general properties of the INC have been characterized. However, these characterizations have little application to antiprotons, which release an extraordinarily large amount of energy into the nucleus via the annihilation process.

One of the unique features of interactions with uranium is fission. Because of the large excitation of the parent nucleus and fission fragments expected from antiproton annihilation, the study of neutron emission appears especially attractive. Results on neutron yields and decay angular distributions should offer clues to the degree of excitation of the nucleus and fragments. Previous studies from this and an earlier experiment have resulted

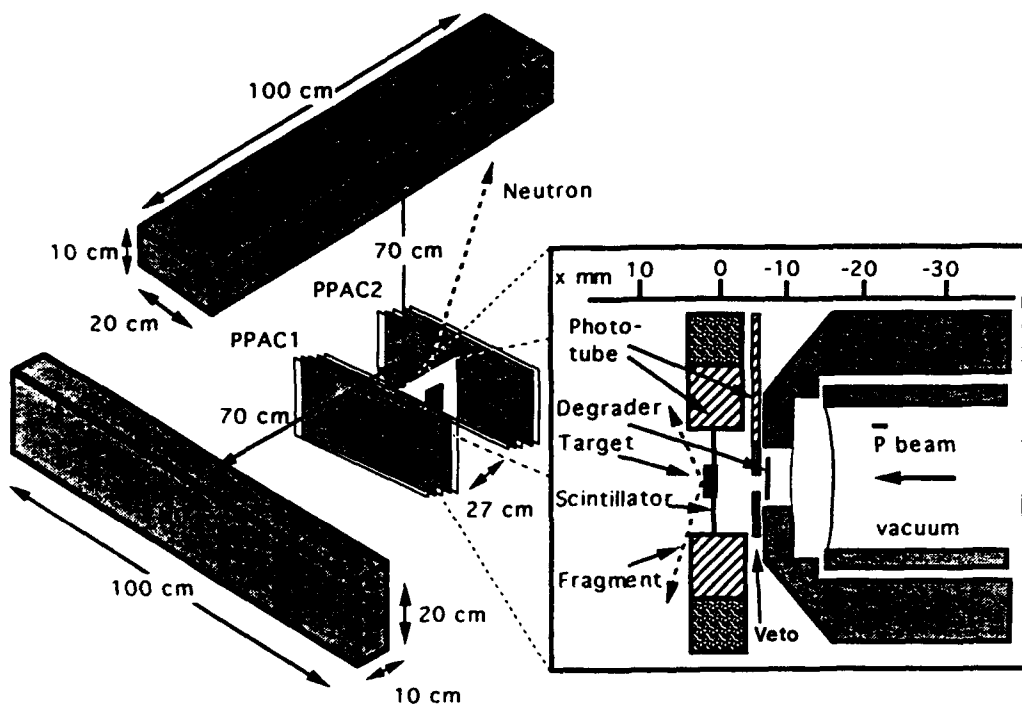


FIG. 1. Schematic layout of target, PPAC, and neutron detectors.

in the first observation of fission neutrons [7] and gamma rays [8], and a detailed measurement of the energy transfer in the INC as deduced from π^0 [9] and charged pion [10] spectra. The goal of this paper is to develop a coherent picture of antiproton-induced fission involving neutron emission, wherein yields and angular distributions are analyzed and discussed.

II. EXPERIMENT

The apparatus is shown schematically in Fig. 1. An antiproton beam with an intensity of 10^5 sec^{-1} and an initial momentum of 105 MeV/c was degraded to rest. About 2% of the antiprotons stopped in a $200\text{-}\mu\text{g}/\text{cm}^2$ natural uranium film deposited on a $200\text{-}\mu\text{m}$ -thick scintillator. Photomultipliers provided a signal for the arrival time of each antiproton. Two parallel-plate avalanche chambers (PPAC 1,2) measured the direction of fission fragments emerging from the target. The target and PPAC's were enclosed in a vacuum box (not shown). In this analysis, valid hits in all four PPAC planes define an event in which a fission occurred. Further details of the apparatus may be found in Ref. [11].

A pair of neutron counters, $N\emptyset$ and $N9\emptyset$, were located outside the vacuum box, each at a distance of 70 cm from the target. A set of 0.6-cm-thick scintillation veto counters (not shown) placed immediately in front of the neutron counters recorded the presence of charged particles. Pulses in the neutron counters, recorded more than 1 nsec later than prompt pions with no corresponding hits in the veto counters, were identified as neutrons. The neutron detectors are described in further detail in Ref. [7].

III. NEUTRON YIELDS

Figure 2 shows the neutron momentum spectrum deduced from hits in the neutron counters. Numerical values for the data are listed in Table I. The distribution has been corrected for (a) solid angle, (b) counting efficiency, (c) background from secondary interactions, and (d) electronic pileup. Solid-angle and counting efficiency corrections were determined using a Monte Carlo simulation. Neutrons from the uranium target were projected toward the neutron counters. The pulse height resulting from an interaction in the counters was calculated using the techniques of Cecil *et al.* [12], converting energy deposition into equivalent electron energy.

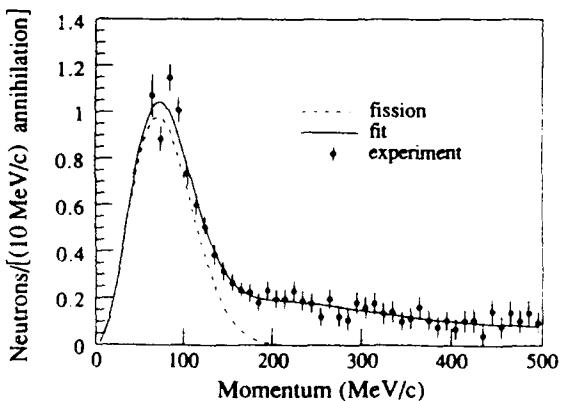


FIG. 2. Measured neutron momentum distribution. The solid line is a three-component fit to the data. The dashed line is the fission component. See text for details.

The cutoff energies for the counters, 0.46 ± 0.02 MeV for $N\emptyset$ and 0.36 ± 0.02 MeV for $N9\emptyset$, were determined by adjusting the simulated spectra to agree with the data for momenta of 50–80 MeV/c.

Background from secondary interactions was measured in runs using a target consisting of a scintillator with no uranium coating. The requirement for fission fragment hits in the PPAC's was removed for these runs. Background subtractions were typically 20% of the data taken with the uranium coating. No hits were observed in $N\emptyset$ or $N9\emptyset$ in 68% of the events. In the remaining events, hits were observed mostly ($\sim 90\%$) due to prompt pions and gamma rays. Since the time-to-digital converters

TABLE I. Experimental data (Fig. 2). Units are number of neutrons per 10 MeV/c per annihilation.

Momentum	Data	\pm error
65	1.0719	0.0924
75	0.8862	0.0547
85	1.1477	0.0586
95	1.0103	0.0556
105	0.7377	0.0506
115	0.6018	0.0475
125	0.5058	0.0463
135	0.3885	0.0430
145	0.3164	0.0405
155	0.2681	0.0395
165	0.2338	0.0385
175	0.2253	0.0434
185	0.1835	0.0389
195	0.2345	0.0416
205	0.1980	0.0396
215	0.1971	0.0436
225	0.2331	0.0437
235	0.1920	0.0456
245	0.1795	0.0426
255	0.1221	0.0413
265	0.1989	0.0462
275	0.1230	0.0435
285	0.1087	0.0458
295	0.1838	0.0482
305	0.1610	0.0492
315	0.1804	0.0482
325	0.1357	0.0482
335	0.1436	0.0483
345	0.1025	0.0421
355	0.1157	0.0474
365	0.1631	0.0498
375	0.1090	0.0459
385	0.0803	0.0470
395	0.1070	0.0446
405	0.0703	0.0462
415	0.1059	0.0495
425	0.1088	0.0510
435	0.0438	0.0500
445	0.1485	0.0533
455	0.0823	0.0504
465	0.1423	0.0581
475	0.1059	0.0503
485	0.1398	0.0556
495	0.0984	0.0479

recorded only the first of multiple hits, the neutron yields shown in Fig. 2 have been multiplied by 1/0.68 to correct for pileup effects.

The neutron spectrum is expected to be composed of high-momentum neutrons from direct knockout INC processes, and low-momentum neutrons from evaporation and fission [7]. The fit (solid curve) in Fig. 2 is the sum of three components: fission (post-scission), evaporation (pre-scission), and direct (pre-scission) neutrons:

$$\frac{dN}{dp} = a_F \beta \frac{e^{-E_F/T_F}}{(\pi E_F T_F)^{1/2}} \sinh(2\sqrt{E_F E}/T_F) e^{-E/T_F} \quad (\text{fission}) \quad (1)$$

$$+ a_{EV} \beta \frac{2\sqrt{E} e^{-E/T_{EV}}}{\sqrt{\pi T_{EV}^{3/2}}} \quad (\text{evaporation}) \quad (2)$$

$$+ a_D \beta \frac{2\sqrt{E} e^{-E/T_D}}{\sqrt{\pi T_D^{-3/2}}} \quad (\text{direct}), \quad (3)$$

where E is the neutron kinetic energy, β is the neutron velocity divided by the speed of light, E_F is the mean fission fragment kinetic energy per u, and T_F , T_{EV} , and T_D are the temperatures of neutrons from the fission, evaporation, and direct processes, respectively. Equation (1) follows from the model of Watt [13]. The yield and temperature parameters found by fitting to the sum of Eqs. (1)–(3) are given in Table II. Yields are integrated so that the factors a_F , a_{EV} , and a_D refer to the number of neutrons per annihilation, from 0 to 1000-MeV/c momentum.

The average atomic number of the fragments from this experiment is $A = 106 \pm 1$ [14]. Therefore, the fragment energy per u (E_F) of 0.74 ± 0.12 MeV corresponds to a kinetic energy of 79 ± 13 MeV, or 158 ± 26 MeV for the sum of the two fragment kinetic energies. This value is in good agreement with the measurement of Bocquet *et al.* [14], where the fission fragment energy was determined directly. A Fermi-gas model of the excited fission fragments relates the excitation energy, E_F^* , to the fragment temperature as [15]

$$E_F^* = a T_F^2 = 51 \pm 10 \text{ MeV}, \quad (4)$$

where the level density parameter $a = A/(10 \pm 1) = 10.6 \pm 1.1 \text{ MeV}^{-1}$. Summing over the two fragments gives 102 ± 20 MeV, which is $22 \pm 5\%$ of the 455 ± 50 MeV previously determined to be transferred to

TABLE II. Fitted neutron yield and temperature parameters. See text for details.

a_D (no./ann)	4.49 ± 0.75
T_D (MeV)	99.6 ± 11.1
a_{EV} (no./ann)	3.40 ± 0.35
T_{EV} (MeV)	18.9 ± 2.0
a_F (no./ann)	8.42 ± 0.25
T_F (MeV)	2.18 ± 0.20
E_F (MeV/nucleon)	0.74 ± 0.12
Total no. neutrons	16.3 ± 0.9

the nucleus from the initial antiproton annihilation [10].

The portion of the fragment excitation energy, which is in the form of fission neutron kinetic energy (dashed curve, Fig. 2), is

$$E_K = (8.42 \pm 0.25) \times \frac{3}{2} (2.18 \pm 0.20) = 28 \pm 3 \text{ MeV}.$$

In addition, nuclear gamma rays account for energy $E_\gamma = 12 \pm 2 \text{ MeV}$ [8]. Therefore, assuming ~ 6 -MeV binding energy for each of the neutrons released, $\sim 88\%$ of the fragment excitation energy is attributed to neutron and gamma-ray emission.

For comparison, the values of these parameters for low-energy neutron-induced fission of uranium are approximately $E_F^* = 21 \text{ MeV}$ [using a temperature of 1.4 MeV in Eq. (4)], $E_K = 5.3 \text{ MeV}$ neutron kinetic energy and $E_\gamma = 10.7 \text{ MeV}$ gamma-ray energy [2,16]. Including ~ 6 MeV binding energy for each of the 2.5 neutrons released, the corresponding fraction of neutron and gamma-ray energy of the total excitation energy is 74%, somewhat smaller than the value for antiproton-induced fission.

IV. NEUTRON ANGULAR DISTRIBUTIONS

The angular distribution of the neutrons with respect to the fragment direction is related to their angular momentum, and to whether they are emitted before or after scission.

Figure 3 shows the laboratory angular distribution between the neutron and fission fragment detected in PPAC-1, for momenta of (a) 60–100 MeV/c and (b) 100–150 MeV/c. Since the apparatus cannot distinguish which fragment emitted the neutron, all spectra are measured with respect to PPAC-1. Geometrical, electronic, and background corrections have been applied on a bin-by-bin basis. The simulation includes a 10-cm rms smearing to account for the spatial resolution of the neutron detectors. The data have been fit (solid line) by a function consisting of three terms, representing decays which are (a) isotropic in the laboratory, allowing for neutrons coming directly from the decay of the parent nucleus before scission, (b) isotropic in the fission fragment rest frame, and (c) characterized by a $\cos^2(\theta)$ distribution in the fission fragment rest frame. Due to Lorentz effects, terms (b) and (c) both contribute to nonisotropy in the laboratory frame. The dashed line in Fig. 3 shows the contribution of term (a), which is large (77% of integrated yield) above 100 MeV/c.

The results may be understood by looking at various ratios, such as the fission fraction

$$FF = (b + c) / (a + b + c), \quad (5)$$

which should be equal to unity if all neutrons emerge after scission. In Table III we show this ratio, which is also plotted in Fig. 4 (open circles), as a function of the neutron momentum. Also shown in Fig. 4 are the results of fits to the momentum spectrum (solid circles) discussed previously. We see that, for momenta below 100 MeV/c, both sets of data are consistent with 100% post-scission neutron emission. However, in the interval 100–150 MeV/c, there is clear evidence for pre-scission neutrons.

TABLE III. Parameters resulting from fits to neutron angular distribution versus neutron momentum. See text for details.

Momentum (MeV/c)	FF	A	$\chi^2/\text{deg freedom}$
60–80	1.060 ± 0.165	0.171 ± 0.081	0.69
80–100	0.800 ± 0.125	0.287 ± 0.132	1.12
100–150	0.232 ± 0.092	0.571 ± 0.776	0.88
150–200	-0.044 ± 0.127		0.54
200–300	0.072 ± 0.070		1.05
300–500	-0.036 ± 0.089		0.80

The spectrum is completely dominated by pre-scission neutrons above approximately 150 MeV/c (12-MeV kinetic energy). A measurement with 155-MeV protons [6] gives a ratio of post-scission to pre-scission neutrons of 0.88 ± 0.05 for neutrons up to 9-MeV kinetic energy. We find a slightly larger value of 1.08 ± 0.29 for the same neutron energy interval.

In Table III we also show values of the anisotropy

$$A = c/b \quad (6)$$

for the 0–150-MeV/c interval where the data result pri-

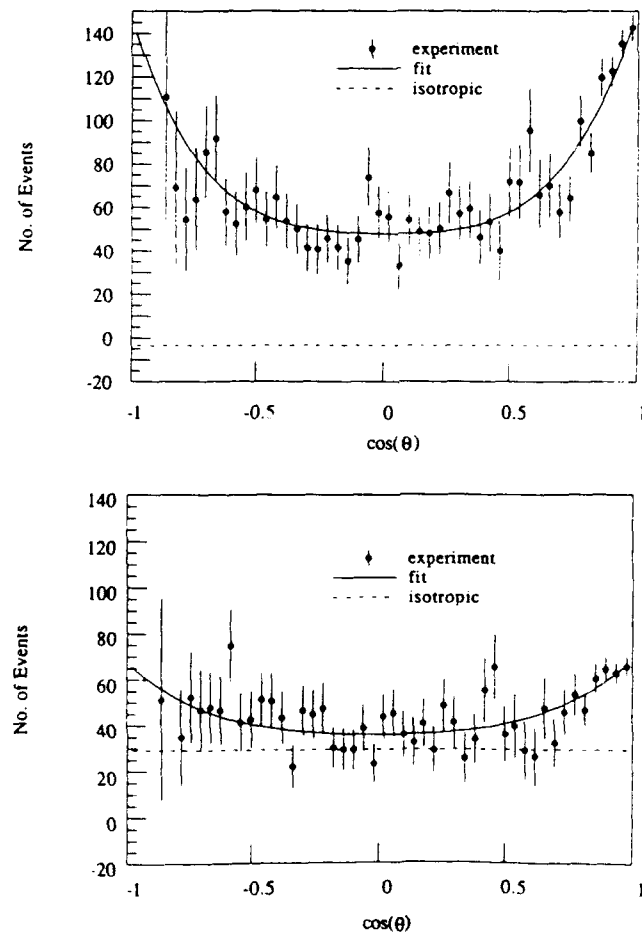


FIG. 3. Neutron laboratory angular distribution for neutron momenta in the range (a) 60–100 and (b) 100–150 MeV/c. The solid lines are fits to the data. The dashed curve is the isotropic part of the fit. See text for details.

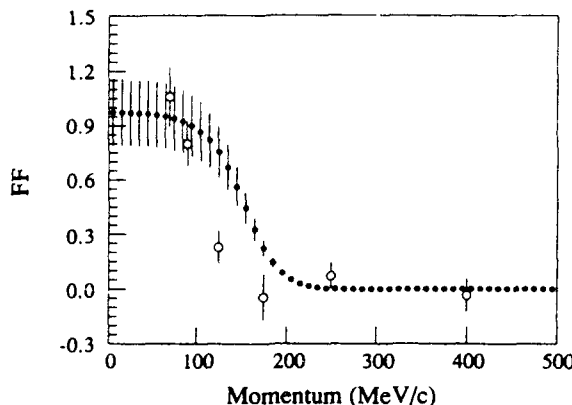


FIG. 4. Fraction of events attributed to fission vs neutron momentum. The (open) solid points are the fraction based on fits to (angular) momentum distributions.

marily from fission. The anisotropies found in our data are substantially larger than those observed (10–15 %) in spontaneous fission of ^{252}Cf [15]. A measurement of 155 MeV protons [6], where one expects large energy transfer to the nucleus, finds no significant anisotropy of neutrons in the fragment rest frame. This is consistent, as will be shown, with a model in which substantial angular momentum is transferred to the fragment in antiproton-induced fission.

The anisotropy may also be used to deduce the moment of inertia of the decaying fission fragment. Following the analysis of Gavron [17] on angular distributions of neutrons from fission fragments, the anisotropy depends on the dimensionless quantity $B^2 = 2IT/\hbar^2$, where I is the moment of inertia of the nucleus and T is its temperature. By linear extrapolation of Gavron's analysis from values of $(B, A) = (6, 0.075)$ and $(11, 0.15)$, we estimate that $B \approx 15$ for $A = 0.22 \pm 0.08$ (average of first two entries of Table III). Using $T = 2.18$ MeV from Table II, it follows that $2I/\hbar^2$ is approximately 103 MeV $^{-1}$. This value is comparable to the value of 86 MeV $^{-1}$ from Gavron's analysis, assuming $B = 11$ and $T = 1.4$ MeV, which is characteristic of fission fragments due to low-energy neutron-induced or spontaneous fission. For additional comparison, we find that the moment of inertia of a rigid sphere, given by $I = 2/5 AR^2$ with $A = 106$ and $R = 1.3 A^{1/3}$ fm, leads to a value of $2I/\hbar^2 = 78$ MeV $^{-1}$. These comparisons suggest that the difference in anisotropies between antiproton-induced fission and low-energy neutron-induced or spontaneous fission is more related to temperature than to moment of inertia.

Knowledge of the B parameter allows one to estimate the angular momentum of the decaying fission fragment. One may assume that the initial spin distribution is of the form [17]

$$P(J) = (2J + 1) \exp[-J(\pm \frac{1}{2})^2/B^2]. \quad (7)$$

By integrating over this distribution, we find that the average angular momentum for $B = 15$ is $\bar{J} = 13\hbar$. By comparison, we note that the average angular momentum of fission fragments produced in low-energy neutron-induced or spontaneous fission is in the range $(4-8)\hbar$ [18]. In the classical approximation each neutron of average momentum 80 MeV/c emitted from a nucleus of radius 6.2 fm carries away approximately $2.5\hbar$ of angular momentum. Therefore, it is quite plausible that an excited nucleus with $J = 13\hbar$ could decay sequentially on average into 4.2 neutrons ($a_F/2$, see Table II) plus 2.0 gamma rays [8].

V. DISCUSSION

A previous measurement of neutrons from antiproton annihilation at rest in uranium [7] was made, using high-momentum pions and protons in a spectrometer as a trigger, and a neutron counter array 180° opposite to the spectrometer. This measurement reported 5.77 ± 0.16 neutrons/annihilation, less than half the 16.3 ± 0.9 neutrons per annihilation given in Table II. This effect may be qualitatively explained from energy considerations. Because the trigger particle carries away a large energy (typically 400 MeV), in general, the fissioning nucleus, and hence fission fragments, will be in a relatively unexcited state, leading to the emission of fewer neutrons than on average.

Finally, it is of interest to account for nucleons in antiproton-induced fission of uranium. The nucleons observed in this experiment are (1) fission fragments -212 ± 2 , (2) evaporation plus direct neutrons -7.9 ± 0.8 , and (3) fission neutrons -8.4 ± 0.3 , for a total of 228.3 ± 2 nucleons. The initial antiproton, uranium state contains 237 nucleons, leaving 8.7 ± 2.0 nucleons unaccounted for in this experiment. In another experiment, yields of low-energy light nuclei ($p, d, t, \text{He, and Li}$) have been measured for antiproton annihilation at rest in uranium [19,20]. The total number of nucleons reported is 4.5 ± 1.4 , leaving a balance of 4.2 ± 2.5 nucleons. We ascribe this small difference to possible statistical or systematic errors in the measurements.

ACKNOWLEDGMENTS

The authors express their thanks to the builders and operators of LEAR at CERN, whose diligent and inspired efforts enabled the acquisition of the data presented in this paper. We also thank Dr. Joseph Cugnon, Dr. Peter Hofmann, and Dr. David Madland for private discussions concerning the interpretation of the data. This work was supported in part by the U.S. Air Force Office of Scientific Research under Grants Nos. 87-0246 and 91-0302.

[1] P. Jasselette, J. Cugnon, and J. Vandermeullen, Nucl. Phys. **A484**, 542 (1988).
 [2] R. Vandenbosch and J. R. Huizenga, *Nuclear Fission* (Academic, New York, 1973).

[3] H. P. Isaak *et al.*, Nucl. Phys. **A392**, 368 (1983).
 [4] K. H. Hicks, *et al.*, Phys. Rev. C **31**, 1323 (1985).
 [5] E. J. Winhold, P. T. Demos, and I. Halpern, Phys. Rev. **87**, 1139 (1952).

- [6] E. Cheifetz and Z. Fraenkel, *Phys. Rev. C* **2**, 256 (1970).
- [7] A. Angelopoulos *et al.*, *Phys. Lett. B* **205**, 590 (1988).
- [8] T. A. Armstrong, R. Bishop, V. Harris, R. A. Lewis, E. Minor, and G. A. Smith, *Z. Phys. A* **331**, 519 (1988).
- [9] T. A. Armstrong, R. Bishop, V. Harris, R. A. Lewis, E. Minor, and G. A. Smith, *Z. Phys. A* **332**, 467 (1989).
- [10] E. D. Minor, T. A. Armstrong, R. Bishop, V. Harris, R. A. Lewis, and G. A. Smith, *Z. Phys. A* **336**, 461 (1990).
- [11] J. P. Bocquet *et al.*, *Phys. Lett. B* **182**, 146 (1986); J. P. Bocquet *et al.*, *ibid.* **192**, 312 (1987); M. Rey-Campagnolle, *Il Nuovo Cimento* **102A**, 653 (1989); S. Polikanov, *Nucl. Phys.* **A502**, 195c (1989).
- [12] R. A. Cecil, B. D. Anderson, and R. Madey, *Nucl. Instrum. Methods* **161**, 439 (1979).
- [13] B. E. Watt, *Phys. Rev.* **87**, 1037 (1952).
- [14] J. P. Bocquet *et al.*, *Z. Phys. A* (to be published); F. Malek, Ph.D. thesis, l'Université Joseph Fourier, Grenoble, France, 1990.
- [15] D. G. Madland and J. R. Nix, *Nucl. Sci. Eng.* **81**, 213 (1982).
- [16] V. M. Gorbachev, Y. S. Zamyatnin, and A. A. Lbov, *Nuclear Reactions in Heavy Elements* (Pergamon, New York, 1980).
- [17] A. Gavron, *Phys. Rev. C* **13**, 2562 (1976).
- [18] J. B. Wilhelmy, E. Cheifetz, R. C. Jared, S. G. Thompson, and H. R. Bowman, *Phys. Rev. C* **5**, 2041 (1972).
- [19] W. Markiel *et al.*, *Nucl. Phys.* **A485**, 445 (1988).
- [20] P. Hofmann *et al.*, *Nucl. Phys.* **A572**, 669 (1990).

M multinucleon phenomena and proton spectra characterizing antiproton annihilation at rest in nuclei

E.D. Minor, T.A. Armstrong, B. Chen, R.A. Lewis, and G.A. Smith

Laboratory for Elementary Particle Science, Department of Physics, 303 Osmond Laboratory, Pennsylvania State University, University Park, PA 16802, USA

Received November 4, 1991

Spectra of protons with momenta greater than 500 MeV/c following antiproton annihilation at rest in carbon and uranium nuclei have been measured. They are compared to recent results from other experiments and to predictions of an intranuclear cascade model. Evidence is presented for a substantial $B > 0$ component in the annihilation process, and an estimate of the magnitude of that component is made.

PACS: 13.75.Cs; 25.40.Jt; 36.10.-k

1. Introduction

The annihilation of antiprotons with nuclei has been seen in recent years to provide information relevant to both particle and nuclear physics. Annihilation at rest, in particular, has refined our understanding of the strong interaction between matter and antimatter as a direct result of providing a uniformly prepared system (having well defined n and l just prior to annihilation) for exploration of pion-nucleus interactions. For annihilation at rest in carbon and uranium, we have previously published spectra for neutral pions [1], charged pions [2], neutrons [3], and low-energy gamma-rays [4]. This paper presents results for complementary proton spectra, which illustrate other features of the interaction.

The spectra presented here (in the momentum range 500-1400 MeV/c) extend the results of [5] (170-640 MeV/c) for the same nuclei. Results from in-flight interactions, which probe higher density regions of the nucleus prior to annihilation, have been published for these same elements by McGaughey et al. [6]. Results following antiproton annihilation at rest in other nuclei have been published for ^{20}Ne [7], for ^{40}Ca , ^{63}Cu , and $^{92,98}\text{Mo}$ [5], and for ^{14}N and ^{2}H gases [8].

* Work supported in part by the U.S. Air Force Office of Scientific Research under grants 87-0246 and 91-0302 and the U.S. National Science Foundation

From a phenomenological point of view, proton spectra at rest and in flight have considerable significance. Experimental results test predictions of the intranuclear cascade model (INC) [9-12]. Such tests suggest refinements to the model, increasing its usefulness in expressing physical behavior, and improving our understanding of both the higher energy annihilation process and the lower energy nuclear interaction. Interest in proton spectra has increased following recent predictions of multinucleon annihilation. The possibility of antiproton absorption on two or more nucleons ($B > 0$ annihilation) presents an opportunity to simultaneously examine the nature of the strong interaction and the nuclear fringe density. Evidence for this type of interaction has been observed in carbon [6, 12, 13] and deuterium [13, 14]. In the exclusive reaction, measured in [13, 14],

$$\bar{p}NN \rightarrow \pi N, \quad (1)$$

the spectator nucleon momentum in the final state is 1232 MeV/c, suggesting that the population of high energy protons may be a measure of the $B > 0$ component [12], although some claim to refute this argument [15].

For annihilation at rest, the interaction is believed to occur at the fringe of the nucleus where $\rho/\rho_0 \approx 0.1$ (implying an average internucleon spacing of ≈ 4 fm, compared to ≈ 1.9 fm in saturated nuclear matter), and this fact suggests that the likelihood of three-particle spatial coincidence may be quite small. However, large de Broglie wavelengths for slow particles imply an effective range of interaction which rises inversely with decreasing momenta, and this behavior has been observed for slow antiproton annihilation [16, 17]. Additional support for this point of view is provided by the spectrum of photons observed following the absorption of negative pions at rest in nuclei [18]:

$$\pi^- + A \rightarrow \gamma + n + (A-1). \quad (2)$$

Presumably, the pion is absorbed by a single proton ($\pi^- + p \rightarrow \gamma + n$), but the resultant gamma spectrum in the nuclear case is wider than may be accounted for by

nuclear fermi motion alone, suggesting that more than one nucleon participates in the absorption process. Consequently, $B > 0$ annihilations are not precluded even in sparsified regions of the nucleus.

A related issue is the fireball radius in annihilation, found to be $\langle R \rangle = 1.89 \pm 0.06$ fm, using pion-interferometry techniques, and approximately constant between 4 and 25 GeV/c [19]. This radius corresponds, however, to the maximum radius obtained by considering the annihilation cross section at the experimental energies as a geometrical entity. Furthermore, the measurement is relevant only to pion generation and carries no detailed information regarding the range of virtual pions extending the strong force to spectator nucleons. Consequently, only model-dependent studies [15, 20] contradict the possibility that a component of four-momentum transfer to spectator nucleon(s) may accompany the majority of nuclear annihilations.

2. Experimental details

Several previous publications [1–4] have presented details of the detector and targets of this experiment. Except for features specific to the analysis of proton spectra, the discussion here will be summary in nature. As is evident [2], proton tracks in the spectrometer are accurately identified; contamination of the spectra is less than 0.7% throughout the momentum spectrum. Momentum resolution resulting from finite wire spacing and Coulomb scattering is seen to vary from 3 to 7% for protons. The agreement between observed and expected $\delta(m^2)$ reported in [2] results from consideration of factors determining mass resolution: finite time resolution (400 ps, rms) and finite momentum resolution.

The acceptance of the spectrometer is determined by the magnetic field, detector materials present and their geometry, and properties of the target. For light particles (pions), tracks are seen with momenta as low as 100 MeV/c, which limit is dictated by the trajectory radius in the magnetic field. For heavier particles (K, p, d, \dots), ionization energy losses in the target and spectrometer entrance constrain the lower limit of momentum more severely. A proton must traverse a finite thickness of target material (depending on target type and escape angle), a cylindrical wire chamber (CWC), drift chambers $R1$ and $R2$, hodoscope A , multiwire proportional chambers $B, C1$, and $C2$, counters Q and V , and the lead photon converter, prior to entering the spectrometer. Losses incurred in these materials average 21 MeV for protons entering the spectrometer from the carbon target and 24 MeV for those from the uranium target.

In addition to precluding observation of proton spectra below 500 MeV/c, dE/dx losses necessitate a track-by-track correction for momentum loss between the target and the spectrometer, in addition to the acceptance correction applied to spectra required by the magnetic field and the finite aperture of the spectrometer. Furthermore, normalization (to particle multiplicity per annihilation) requires consideration of that fraction of pro-

tons which are detected by the CWC (and thus counted in the event multiplicity), but which are not sufficiently energetic to enter the spectrometer and form a valid trigger. Such events occur predominantly, but not exclusively, for protons below 500 MeV/c, where energy distributions have recently been published [5]. In addition, a small number of tracks at higher momenta enter detector materials at large angles to the normal, traverse significant distances through solid matter, and range. A Monte Carlo simulation of the detector has been used in both cases to determine the fraction of these counted but unseen tracks, using spectra from [5] for the lower-momentum tracks, and using our measured spectra (iteratively) for the higher-momentum ones. From these simulations, we estimate that the multiplicity of protons detected by the CWC, but physically unable to enter the spectrometer, is 0.189 ± 0.032 (0.203 ± 0.035) per annihilation for carbon (uranium).

3. Results

Figure 1 (a, b) and Table 1 present our measured proton spectra for carbon and uranium, and Table 2 summarizes the total multiplicities observed. Also presented in Fig. 1 are results from [5] for these nuclei, which demonstrate agreement at the 15% (19%) level for carbon (uranium) in the common region (500–640 MeV/c) of the two meas-

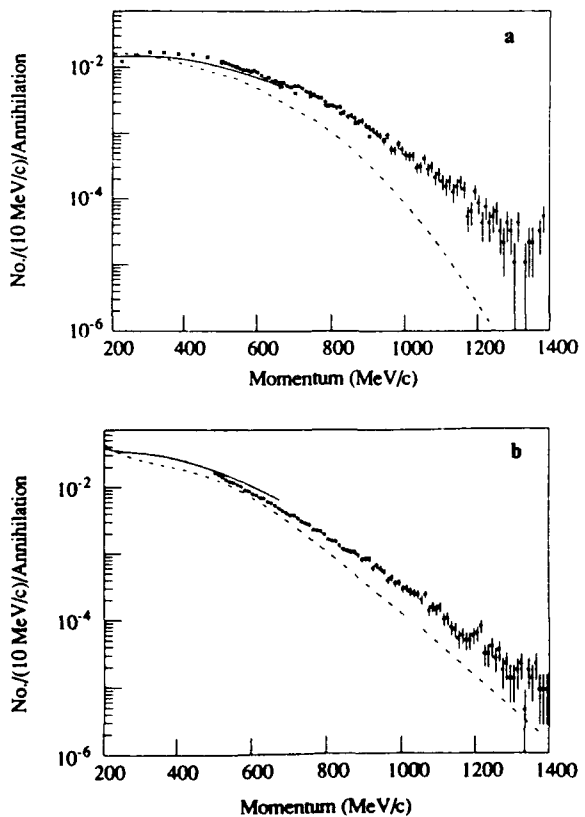


Fig. 1. Proton yield per 10 MeV/c interval per annihilation for carbon **a** and uranium **b**. Circles with error bars: this experiment; solid curve: data from [5]; crosses: data from [8] (nitrogen); dashed curve: results from the LAHET model [9, 23].

Table 1. Number of protons per 10 MeV/c per annihilation

Momentum (MeV/c)	Yield		Yield	
	Carbon	Error	Uranium	Error
505	0.116 E-01	0.469 E-03	0.158 E-01	0.429 E-03
515	0.116 E-01	0.464 E-03	0.147 E-01	0.403 E-03
525	0.111 E-01	0.446 E-03	0.136 E-01	0.380 E-03
535	0.104 E-01	0.434 E-03	0.125 E-01	0.360 E-03
545	0.101 E-01	0.421 E-03	0.116 E-01	0.341 E-03
555	0.958 E-02	0.419 E-03	0.114 E-01	0.338 E-03
565	0.904 E-02	0.406 E-03	0.106 E-01	0.326 E-03
575	0.903 E-02	0.403 E-03	0.100 E-01	0.314 E-03
585	0.855 E-02	0.391 E-03	0.884 E-02	0.295 E-03
595	0.890 E-02	0.395 E-03	0.852 E-02	0.291 E-03
605	0.830 E-02	0.385 E-03	0.773 E-02	0.268 E-03
615	0.751 E-02	0.366 E-03	0.739 E-02	0.264 E-03
625	0.665 E-02	0.342 E-03	0.681 E-02	0.247 E-03
635	0.704 E-02	0.355 E-03	0.667 E-02	0.244 E-03
645	0.621 E-02	0.332 E-03	0.593 E-02	0.226 E-03
655	0.618 E-02	0.327 E-03	0.570 E-02	0.216 E-03
665	0.579 E-02	0.325 E-03	0.522 E-02	0.207 E-03
675	0.583 E-02	0.323 E-03	0.472 E-02	0.192 E-03
685	0.526 E-02	0.305 E-03	0.437 E-02	0.182 E-03
695	0.496 E-02	0.298 E-03	0.406 E-02	0.174 E-03
705	0.523 E-02	0.301 E-03	0.372 E-02	0.165 E-03
715	0.520 E-02	0.299 E-03	0.377 E-02	0.166 E-03
725	0.477 E-02	0.289 E-03	0.341 E-02	0.157 E-03
735	0.432 E-02	0.277 E-03	0.302 E-02	0.146 E-03
745	0.411 E-02	0.268 E-03	0.285 E-02	0.141 E-03
755	0.377 E-02	0.258 E-03	0.272 E-02	0.139 E-03
765	0.348 E-02	0.256 E-03	0.227 E-02	0.126 E-03
775	0.340 E-02	0.244 E-03	0.224 E-02	0.126 E-03
785	0.296 E-02	0.229 E-03	0.218 E-02	0.127 E-03
795	0.257 E-02	0.215 E-03	0.195 E-02	0.123 E-03
805	0.262 E-02	0.214 E-03	0.164 E-02	0.114 E-03
815	0.243 E-02	0.206 E-03	0.155 E-02	0.111 E-03
825	0.247 E-02	0.207 E-03	0.153 E-02	0.109 E-03
835	0.208 E-02	0.195 E-03	0.132 E-02	0.100 E-03
845	0.176 E-02	0.176 E-03	0.115 E-02	0.917 E-04
855	0.185 E-02	0.177 E-03	0.110 E-02	0.899 E-04
865	0.167 E-02	0.172 E-03	0.105 E-02	0.874 E-04
875	0.146 E-02	0.164 E-03	0.102 E-02	0.886 E-04
885	0.154 E-02	0.162 E-03	0.931 E-03	0.847 E-04
895	0.130 E-02	0.151 E-03	0.796 E-03	0.801 E-04
905	0.121 E-02	0.142 E-03	0.823 E-03	0.811 E-04
915	0.110 E-02	0.142 E-03	0.809 E-03	0.804 E-04
925	0.996 E-03	0.134 E-03	0.581 E-03	0.650 E-04
935	0.910 E-03	0.127 E-03	0.644 E-03	0.670 E-04
945	0.753 E-03	0.120 E-03	0.571 E-03	0.628 E-04
955	0.922 E-03	0.124 E-03	0.510 E-03	0.573 E-04
965	0.566 E-03	0.101 E-03	0.380 E-03	0.478 E-04
975	0.551 E-03	0.973 E-04	0.417 E-03	0.513 E-04
985	0.678 E-03	0.108 E-04	0.342 E-03	0.451 E-04
995	0.564 E-03	0.942 E-04	0.351 E-03	0.452 E-04

Table 1 (continued)

Momentum (MeV/c)	Yield		Yield	
	Carbon	Error	Uranium	Error
1005	0.465 E-03	0.858 E-04	0.281 E-03	0.395 E-04
1015	0.451 E-03	0.831 E-04	0.290 E-03	0.407 E-04
1025	0.450 E-03	0.834 E-04	0.255 E-03	0.375 E-04
1035	0.295 E-03	0.665 E-04	0.240 E-03	0.360 E-04
1045	0.309 E-03	0.681 E-04	0.229 E-03	0.355 E-04
1055	0.407 E-03	0.789 E-04	0.290 E-03	0.315 E-04
1065	0.281 E-03	0.647 E-04	0.228 E-03	0.349 E-04
1075	0.308 E-03	0.679 E-04	0.132 E-03	0.259 E-04
1085	0.210 E-03	0.555 E-04	0.151 E-03	0.276 E-04
1095	0.238 E-03	0.593 E-04	0.136 E-03	0.262 E-04
1105	0.182 E-03	0.514 E-04	0.150 E-03	0.277 E-04
1115	0.154 E-03	0.472 E-04	0.978 E-04	0.219 E-04
1125	0.181 E-03	0.513 E-04	0.102 E-03	0.223 E-04
1135	0.125 E-03	0.424 E-04	0.739 E-04	0.188 E-04
1145	0.153 E-03	0.469 E-04	0.690 E-04	0.181 E-04
1155	0.181 E-03	0.512 E-04	0.504 E-04	0.154 E-04
1165	0.139 E-03	0.446 E-04	0.568 E-04	0.157 E-04
1175	0.532 E-04	0.238 E-04	0.480 E-04	0.145 E-04
1185	0.638 E-04	0.260 E-04	0.480 E-04	0.145 E-04
1195	0.128 E-04	0.368 E-04	0.568 E-04	0.157 E-04
1205	0.851 E-04	0.301 E-04	0.611 E-04	0.163 E-04
1215	0.425 E-04	0.213 E-04	0.786 E-04	0.185 E-04
1225	0.744 E-04	0.281 E-04	0.306 E-04	0.116 E-04
1235	0.425 E-04	0.213 E-04	0.306 E-04	0.116 E-04
1245	0.532 E-04	0.238 E-04	0.393 E-04	0.131 E-04
1255	0.638 E-04	0.260 E-04	0.262 E-04	0.107 E-04
1265	0.319 E-04	0.184 E-04	0.349 E-04	0.124 E-04
1275	0.213 E-04	0.150 E-04	0.175 E-04	0.873 E-05
1285	0.425 E-04	0.213 E-04	0.218 E-04	0.977 E-05
1295	0.319 E-04	0.184 E-04	0.131 E-04	0.756 E-05
1305	0.106 E-04	0.106 E-04	0.131 E-04	0.756 E-05
1315	0.425 E-04	0.213 E-04	0.175 E-04	0.873 E-05
1325			0.218 E-04	0.977 E-05
1335	0.106 E-04	0.106 E-04	0.437 E-04	0.437 E-05
1345	0.213 E-04	0.150 E-04	0.175 E-04	0.873 E-05
1355	0.213 E-04	0.150 E-04	0.131 E-04	0.756 E-05
1365			0.218 E-04	0.977 E-05
1375	0.319 E-04	0.184 E-04	0.873 E-05	0.618 E-05
1385	0.532 E-04	0.238 E-04	0.873 E-05	0.618 E-05
1395			0.873 E-05	0.618 E-05
1405	0.106 E-04	0.106 E-04		
1415			0.437 E-05	0.437 E-05
1425			0.437 E-05	0.437 E-05
1435				
1445				
1455			0.437 E-05	0.437 E-05
1465				
1475	0.106 E-04	0.106 E-04		
1485	0.106 E-04	0.106 E-04		
1495				

urements. In addition, results are presented in Fig. 1a (carbon) for nitrogen, [8], which confirm that no substantial difference exists between these two nuclei for inclusive measurements. The original INC code of Yariv and Fraenkel, ISABEL [21, 22], has been modified [9] and predictions of a recently updated version, LAHET [23], are presented for comparison. It is clear that the model's spectra differ significantly from the data for both nuclei, especially at the higher momenta, while the integrated multiplicities are underestimated by 20–25% (Table 2). The deficiencies in the model's spectra at the

higher momenta are similar to those seen for in-flight interactions [6], but are much larger in the present case. The deficiency increases with increasing momentum, and exceeds an order of magnitude for carbon near 1100 MeV/c. The discrepancy is smaller for uranium but is still significant, especially at the higher momenta.

This experiment finds an increase in the total proton yield measured by [5] of 20% for carbon and 9% for uranium above 640 MeV/c. While the increases in multiplicity are modest, the increase in energy carried off by ejected protons is significant: 30 MeV (+ 64%) per an-

Table 2. Integrated proton multiplicities per \bar{p} annihilation at rest. Results from this experiment and from [5] are combined on the third line. (The differential yields from the two experiments have been summed. Both experiments have measured the region between 500 and 640 MeV/c, and their average yield was taken prior to summing). Where two errors are stated, the first is statistical, the second systematic; a single error, when given, has combined the individual contributions

Target	Carbon	Uranium
500–1400 MeV/c, this experiment	0.235 ± 0.002 ± 0.041	0.225 ± 0.001 ± 0.036
170–640 MeV/c, [5]	0.60 ± 0.04	1.23 ± 0.39
170–1400 MeV/c, combining rows 1 and 2	0.721 ± 0.053	1.34 ± 0.037
170–1400 MeV/c, the LAHET model [9]	0.573	1.0283

nihilation for carbon and 21 MeV (+ 25%) for uranium. Perhaps more important, this region of the spectra opens a new window on the physics of \bar{p} annihilation in nuclei, as will be discussed in following sections.

4. Discussion

A. The intranuclear cascade model

The LAHET model simulates a localized $\bar{p}N$ interaction, suggested by pion-interferometry experiments [19] to occur in a volume of radius $\langle R \rangle = 1.89 \pm 0.06$ fm at high \bar{p} energies. For each annihilation, a number of pions (five, on average) is chosen consistent with the multiplicity distribution of [24] and momenta are assigned to each primordial pion using the statistical phase-space model of [25]. The momentum distribution compares reasonably well to the distribution measured in [26]. It peaks, however, at a higher momentum ($\simeq 340$ MeV/c compared to $\simeq 250$ MeV/c for the data), and the peak is narrower. As a consequence, for momenta greater than $\simeq 600$ MeV/c, the measured differential multiplicities of pions are twice as great as the model's predictions [9].

The primordial pions generated by the annihilation propagate through space-time, and may undergo uncorrelated interactions with the nucleons comprising the nucleus. Pion-nucleon interactions are treated in the isobar model, using an energy-dependent width for the Δ . The nucleons populate an ideal Fermi gas, with a sharp cutoff at the Fermi momentum.

Previous applications of this model tested in-flight interactions, characterized by the \bar{p} impinging on the nucleus at randomly-selected impact parameters. In order to simulate events occurring from atomic orbits, we have calculated the shape of the overlap between the nuclear wave function (approximated by a Wood-Saxon density distribution) and the hydrogenic wave function for an antiproton in an $n=3$, $l=2$ (carbon) or $n=9$, $l=8$ (uranium) orbit [2, 27]. A selection of radii, representative of the overlap region, were chosen and used as impact parameters of different runs of the LAHET code. The

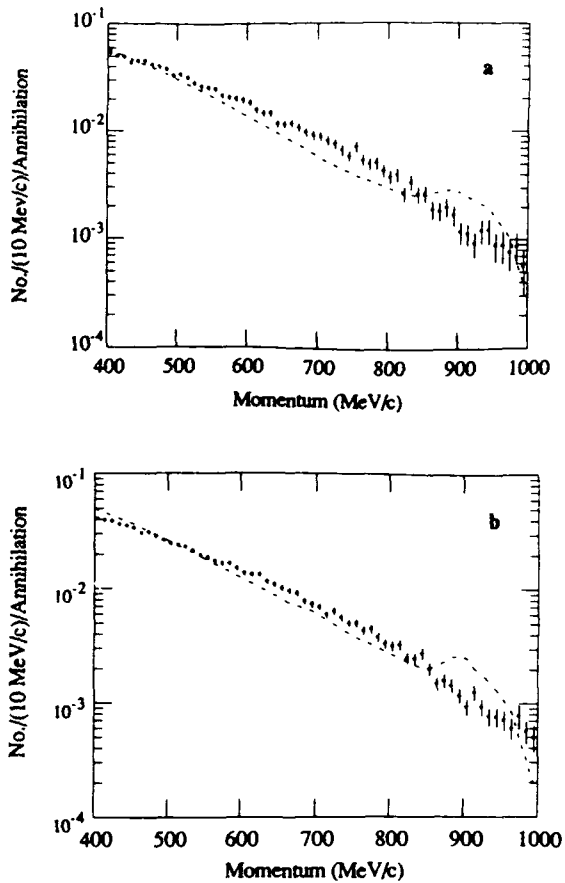


Fig. 2. Pion yield per 10 MeV/c interval per annihilation for carbon **a** and uranium **b**. Circles with error bars: data from [2]; dashed curve: results from the LAHET model [9, 23]

results of each run were weighted according to the magnitude of the overlap at the corresponding radius and all runs for a given target nucleus were combined.

One difficulty with the LAHET model is illustrated in Fig. 2, where structures appear in the predicted pion spectra for both carbon and uranium near 920 MeV/c. No evidence of comparable structure is apparent in the measured result shown in the same figures [2]. Presumably, these structures result from $\bar{p}N \rightarrow \pi\pi$, as observed by the same detector with a deuterium target [28] at a rate $\simeq 0.009$ per annihilation. In measurements with heavy targets, tight cuts are required on event topology to bring out a small structure in the carbon data [13] corresponding to 10^{-4} per annihilation. In the LAHET model, \bar{p} annihilation occurs on the nuclear surface with the remaining spectator nucleus recoiling with the Fermi momentum of the annihilated nucleon, thus producing a smearing in the momentum distribution of the primordial pions. A pion has $\simeq 20\%$ chance of impinging on the nucleus, leaving 80% of all pions to retain the momentum acquired at the instant of annihilation. The extreme depletion of the $\pi\pi$ line in carbon (by a factor of 90) and its absence in uranium suggests that the model of the nucleus as spectator during the annihilation process underestimates the role of neighboring nucleons. The $\pi\pi$

line is smeared beyond detection, presenting the possibility of an interaction with one or more neighboring nucleons as a factor in nearly every annihilation.

B. The $B > 0$ interaction

1. *Evidence for $B > 0$ annihilations.* Figure 3 illustrates an interesting feature of the carbon and uranium proton spectra. The multiplicity of protons in uranium, which is much greater than that for carbon below 500 MeV/c, falls off more rapidly than does carbon with increasing momentum. At ≈ 620 MeV/c, the two are equal, with the uranium multiplicity falling sharply relative to carbon multiplicity until, near 800 MeV/c, it reaches approximately 60% that of carbon. This fraction is then nearly constant through 1200 MeV/c (at which point statistics become inadequate). Below 800 MeV/c, this phenomenon is consistent with behavior reflecting multiple scattering effects characterized by temperature [5]: 99.1 ± 3.6 MeV for carbon and 76.1 ± 2.3 MeV for uranium. However, the LAHET model does not predict an excess of protons from carbon above those from uranium at high momentum: above 800 MeV/c, the carbon multiplicity remains at 60–80% of the uranium multiplicity in the LAHET model. Furthermore, the constancy of the ratio between the measured multiplicities above 800 MeV/c is inconsistent with both the multiple scattering mechanism and the temperature parametrization (which results in an exponential curve for the ratio as a function of energy). Consequently, it is worth considering other possible mechanisms which might lead to the observed behavior.

Many authors have discussed the high-energy tail seen in proton spectra following β annihilation on nuclei. Some have attempted, using previously available data [6], to account for the observed tail by assuming the existence of $B > 0$ interactions [12], while other authors have argued against this mechanism and shown that the tail might be understood by taking into account the Hulthén momentum distribution which characterizes bound nucleons

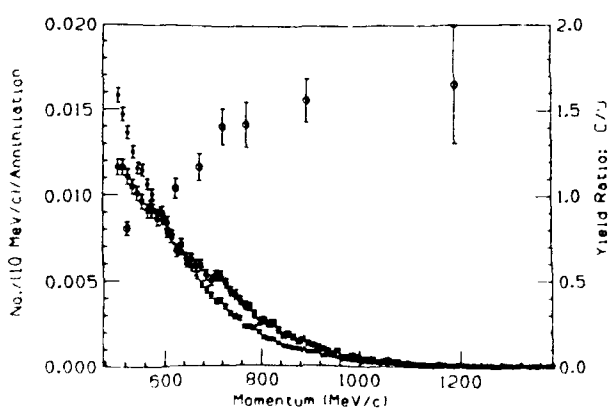


Fig. 3. *Left scale:* proton yield per 10 MeV/c interval per annihilation. Squares: carbon; diamonds: uranium. *Right scale (circles):* carbon yield divided by uranium yield, with bins combined to reduce statistical errors

[20] or by using a suitable phenomenological INC code [15]. Arguments both for and against the $B > 0$ hypothesis have, in general, relied on ad hoc revisions to existing INC models. Model-independent experimental evidence supporting or disclaiming the hypothesis is lacking except for certain rare exclusive reactions [14].

In the search for such evidence, we have observed that primordial particles (including annihilation pions and, possibly, “spectator” nucleons participating in a $B > 0$ annihilation) differ from directly ejected nucleons in a fundamental way. Primordial particles may interact with the nucleus and be absorbed or degraded in momentum, removing them from the range of measurement or from the higher regions of the spectrum. By contrast, INC-generated nucleons are created by the nuclear interaction. Thus, those primordial particles which survive to be measured at their original momentum will contain an approximate factor $(1 - \Omega/4\pi)$ relative to their original population, where Ω is the solid angle subtended by the nucleus at the annihilation point. Consequently, the primordial population decreases with increasing A . On the other hand, nucleons ejected during the INC process, if they could be identified, will exhibit populations which are complex, non-linear functions of A and λ (the average length of nuclear matter traversed), monotonically increasing with those parameters as do the integrated multiplicities for carbon and uranium.

Presumably, the majority of pions above a few hundred MeV/c are primordial for annihilation at rest, although their momentum may have been degraded as a result of nuclear interaction. For an estimate, we select the annihilation point to lie one fm outside the nuclear half-density radius given by $R = 1.2 A^{1/3}$ [29]; the nuclear solid angle is subtended by a sharp-edged sphere of radius R centered on the nucleus. With the chosen geometry, the subtended solid angles (as a fraction of 4π) are 0.16 for carbon and 0.26 for uranium. Thus, the multiplicity of primordial pions of all charge, $dM_\pi(p)/dp$, is given by

$$\left(\frac{dM_\pi(p)}{dp} \right)_{\text{primordial}} = \frac{M_\pi^0 + M_\pi^\pm}{M_\pi^\pm} \frac{1}{1 - \Omega/4\pi} \left(\frac{dM_\pi^\pm(p)}{dp} \right)_{\text{measured}}, \quad (3)$$

where the factor relating all pions to charged pions is calculated from the method outlined in [30]; the multiplicities of charged pions have been measured in [2]. There is no a priori reason to suspect that the primordial pion multiplicities differ between carbon and uranium annihilations, since they are thought to be mainly a function of available center-of-mass energy. Consequently, the ratio of primordial pion multiplicities,

$$R = \left(\frac{dM_\pi^C(p)}{dp} \right) / \left(\frac{dM_\pi^U(p)}{dp} \right), \quad (4)$$

should be a value close to one, resulting from the cancellation of systematic errors in this estimate. Figure 4a illustrates the result of this calculation for experimental

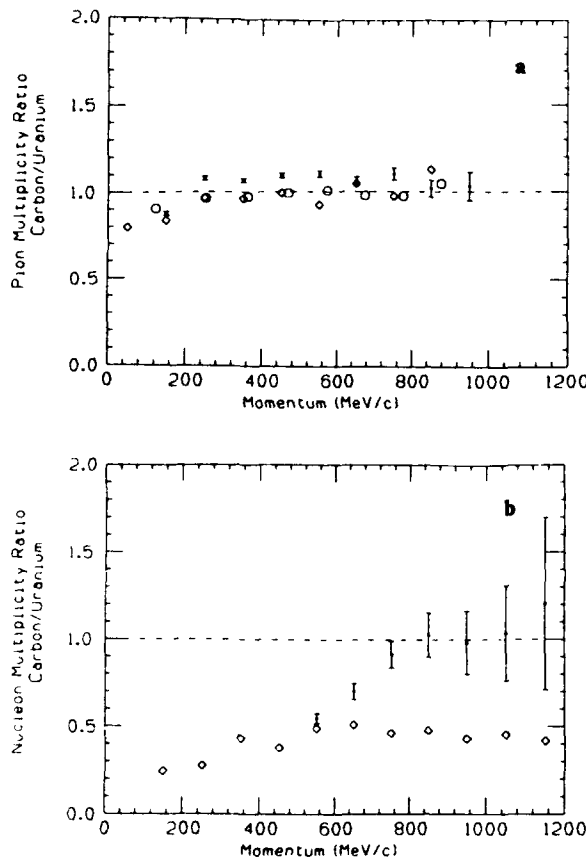


Fig. 4a, b. The ratio R between corrected multiplicities for carbon and uranium. See text. a Pions. Squares with error bars: this experiment; diamonds: results from the LAHET model [9, 23]; circles: results from the INC model of [2, 31]. b Nucleons. Squares with error bars: this experiment; diamonds: results from the LAHET model [9, 23]

data [2] and for two sets of pion predictions, one from LAHET and one from [31]. Both INC results, as well as the data, are seen to produce horizontal lines very close to unity above 300 MeV/c, as expected for primordial entities. Below that momentum, contributions are present from INC pion production which is manifestly A -dependent.

A search for similar behavior in the proton high-momentum tails has been done using the spectra from this experiment. In this case, the spectrum is expected to contain INC protons as well as any resulting from $B > 0$ annihilations, especially at lower momenta. Furthermore, the correction for neutral particles must be replaced in (3) to account for unobserved neutrons. We have used $(N + Z)/N$, which ignores deviations resulting from possible different cross sections for the spectator neutron and spectator proton processes. The importance of these corrections is very much reduced when the ratio is taken. We presume that the likelihood of a $B > 0$ interaction depends mainly on $\rho(\mathbf{r})$ [12] at the annihilation site as does the likelihood of annihilation in the first place. Consequently, we expect the total $B > 0$ multiplicity, as well as the spectrum of $B > 0$ nucleons, to be constant across various nuclei.

Figure 4b shows the results of the calculation for the data as well as for the INC prediction provided by LAHET. The data show asymptotic behavior, with $R = 0.5$ at 500 MeV/c and rising to unity at 800 MeV/c, where it remains constant until 1200 MeV/c. The model, on the other hand, shows nearly constant behavior, with $R \approx 0.5$ above 300 MeV/c.

Not only are experimental and calculational errors cancelled in this approach, but so are natural factors such as the existence of a high-energy tail in the Fermi distribution. The Fermi momenta are comparable for carbon (250 MeV/c) and uranium (229 MeV/c) [20], which suggests that multiplicities of nucleons present with higher momenta are most likely comparable as well. We consider Fig. 4b to be strong evidence supporting the view that proton spectra above 800 MeV/c are dominated by the $B > 0$ component. It is evident, in any case, that a natural process is at work which is not reflected in our present concept of the INC model.

2. *Estimating the $B > 0$ component.* Having established the nature of the high-momentum tail in proton spectra, it is now feasible to estimate the magnitude of the $B > 0$ component. Some fraction of the high-momentum tail is due to INC processes, and is predicted by LAHET, while an additional fraction may be due to a long tail in nucleon Fermi energies [15, 20], which LAHET does not take into account. For a quantitative estimate, we have chosen to use the LAHET model to calculate the INC component, and assign the difference between measurement and prediction to the $B > 0$ component, thus ignoring the Hulthén tail of the nucleon energies.

Shortcomings of this model are well-known and have been discussed elsewhere [6, 9, 15, 20]. In addition to the sharp cutoff of nucleon momenta at the Fermi energy, the nuclear Fermi gas model is known to be inadequate at the nuclear surface [32], where annihilations at rest are occurring. Furthermore, the criticisms of the primordial pion spectrum mentioned earlier must not be overlooked, since the resultant INC proton spectrum can, at best, reflect that primordial spectrum. These points generally imply that LAHET underestimates high-energy proton production resulting from INC processes. Consequently, by ascribing the excess seen above the LAHET prediction to $B > 0$, we are calculating an upper limit on the latter component.

Hernandez and Oset [12] have shown that the expected $B > 0$ spectrum is a phase space distribution containing components for $B = 1, 2, 3, \dots$ folded in with components resulting from $n_\pi = 2, \dots$, where n_π is the number of real and virtual pions produced in the annihilation. The amplitude of the phase space component relevant to each combination of B and n_π is parametrized from theoretical considerations. The mixing factors, $R_n P_n$, $S_n P_n$, and $T_n P_n$, from [12], determine the contributions from $B = 1, 2, 3$, respectively, for n primordial pions:

$$\Gamma^{(B=1)} = \Gamma^{(\pi)} \left(\sum_n P_n R_n \right) \left(\frac{\rho}{\rho_0} \right) \quad (5)$$

$$\Gamma^{(B=2)} = \Gamma^{(\pi)} \left(\sum_n P_n S_n \right) \left(\frac{\rho}{\rho_0} \right)^2 \quad (6)$$

Table 3. The extrapolated values of the mixing factors $R_n P_n$, $S_n P_n$, and $T_n P_n$, where n is the multiplicity of real and virtual pions, as described in [12]. See text

n	$R_n P_n$	$S_n P_n$	$T_n P_n$
2	0.0003637	0.0000092	0.0000000
3	0.0397200	0.0036480	0.0000907
4	0.2820000	0.0998000	0.0091200
5	1.6100000	1.6520001	0.4852000
6	1.7420000	4.2160001	3.9020000
7	0.9240000	5.1619997	9.5600004

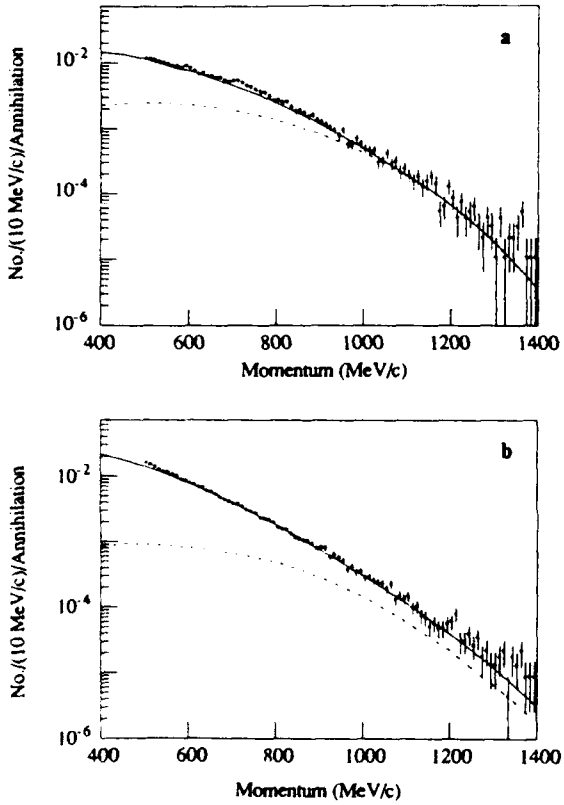


Fig. 5. Proton yield per 10 MeV/c interval per annihilation for carbon **a** and uranium **b**. Circles with error bars: this experiment; dashed curve: the renormalized $B > 0$ spectrum; solid curve: results from the LAHET model [9, 23] added to the renormalized $B > 0$ spectrum

$$\Gamma^{(B=3)} = \Gamma^{(\pi)} \left(\sum_n P_n T_n \right) \left(\frac{\rho}{\rho_0} \right)^3. \quad (7)$$

These parameters are determined for annihilation in flight in [12] and we have extrapolated them to the situation at rest. Table 3 presents the extrapolated values. For each value of B and n_n , a phase space for ejected nucleons has been calculated using the CERN program FOWL [33]. By combining these spectra using the extrapolated mixing factors, it is possible to produce a curve expected for the $B > 0$ component. The mixing constants have been applied assuming that $\rho/\rho_0 = 0.1$ at the point of annihilation [27]. The phase space curve generated by using this prescription is renormalized to account for the dif-

ference between measurement and prediction in the 1000–1200 MeV/c region, where our statistics are good. The renormalized curve is then integrated over all momenta to find the $B > 0$ multiplicity per event.

The results are illustrated in Fig. 5, where the $B > 0$ component is shown separately as well as combined with the LAHET prediction for comparison with the data. The fit throughout our measured momentum range is excellent. We find 0.146 ± 0.015 (0.054 ± 0.007) $B > 0$ protons per annihilation for carbon (uranium). In order to calculate the fraction of events which are due to $B > 0$ interactions, three corrections are applied. First, the values are multiplied by a factor to correct for nuclear absorption. We have used the nuclear solid angle approximation previously described to do this. Second, neutrons are accounted for by multiplying by $(N+Z)/Z$. Using formulae developed in [12], the nuclear densities (ρ/ρ_0) at the point of annihilation are found to be 0.057 ± 0.004 (carbon) and 0.033 ± 0.003 (uranium). Third, the $B > 0$ phase space spectrum contains 79% $B = 1$, 19% $B = 2$, and 1.4% $B = 3$, which must be unfolded. After including these corrections, we observe $27 \pm 2\%$ ($15 \pm 2\%$) of all events in carbon (uranium) resulting from $B > 0$ annihilations.

The \bar{p} annihilation at rest is known to occur from the ($n = 3$, $l = 2$) state in carbon [34]. The overlap integral between the antiprotonic wave function for this state and the nuclear density distribution implies an average density in the annihilation region of $\rho/\rho_0 = 0.087$ which is about 60% larger than our measurement. For uranium, the annihilation state has not been published, but our measurement may be compared to average densities calculated from the overlap integrals of 0.143 ($n = 9$, $l = 8$), 0.0803 ($n = 10$, $l = 9$), and 0.0405 ($n = 11$, $l = 10$), and suggests that the annihilation likely occurs from the $n = 10$ or $n = 11$ state. Unfortunately, the radial dependence of the nuclear density in the region $\rho/\rho_0 < 0.1$ is not well established. Consequently, a precise estimate of the annihilation state is not possible.

The difference between the $B > 0$ rates for the two nuclei contradicts our earlier assumption that the multinucleon component should be a constant across various nuclei. A number of possible explanations for this discrepancy exist, including: (1) the wrong state may have been chosen for the antiprotonic atom prior to annihilation in uranium in the simulation (although good agreement for this state is seen in the pion spectra [2]); (2) the LAHET code may be faulty in its representation of the INC process (as already discussed); (3) there may exist some unforeseen physical reason for the difference, possibly resulting from different orbital shapes corresponding to different values of l in the antiprotonic atom prior to annihilation. In regard to this point, the likelihood of the annihilation having occurred is proportional to $f(\rho_{NUC}, \Psi_p) t$, where ρ_{NUC} is the nuclear density and Ψ_p the antiproton atomic wavefunction. An orbit where a smaller nuclear density is experienced by the \bar{p} could still result in annihilation, given sufficient time before the next step in the atomic cascade occurs, and the difference in nuclear density would skew the components of the $B > 0$ phase space model.

5. Conclusions

In presenting measurements of proton spectra following annihilation at rest in carbon and uranium, we have found evidence for the existence of $B > 0$ nuclear annihilations. Support for the point of view where energy is transferred to neighboring nuclei in nearly all annihilations is provided by the highly suppressed (or smeared) $pN \rightarrow \pi\pi$ line in carbon and uranium. Furthermore, the high energy proton tail has been seen to be of constant magnitude between carbon and uranium, once corrected for absorption and unobserved neutrons, implying that such protons are ejected from within the localized annihilation volume, rather than throughout the extent of the nucleus, as the intranuclear cascade model assumes. We have estimated the magnitude of $B > 0$ annihilation rates in carbon and uranium and found them to be $27 \pm 2\%$ and $15 \pm 2\%$, respectively. The reason for the difference between these two values is unclear; some physical possibilities have been cited in the text.

We thank the staff of the CERN PS Division for their dedicated and skillful operation of LEAR during the course of this experiment. In addition, we would like to express our appreciation to Los Alamos National Laboratory, Radiation Transport Group, for generously providing us with the LAHET intranuclear cascade code and, in particular, to Dr. Richard E. Prael for informative and enlightening discussions regarding the operation of the code and the principles underlying its construction.

References

1. Armstrong, T.A., Bishop, R., Harris, V., Lewis, R.A., Minor, E.D., Smith, G.A.: Z. Phys. A - Atomic Nuclei **332**, 467 (1989)
2. Minor, E.D., Armstrong, T.A., Bishop, R., Harris, V., Lewis, R.A., Smith, G.A.: Z. Phys. A - Atomic Nuclei **336**, 461 (1990)
3. Angelopoulos, A., Apostolakis, A., Armstrong, T.A., Bassalleck, B., Bueche, G., Fero, M., Gee, M., Graf, N., Koch, H., Lewis, R.A., Mandelkern, M., Papaelias, P., Poth, H., Rozaki, H., Sakellou, L., Schultz, J., Schwertel, J., Smith, G.A., Usher, T., Wolfe, D.M.: Phys. Lett. **B205**, 590 (1988)
4. Armstrong, T.A., Bishop, R., Harris, V., Lewis, R.A., Minor, E.D., Smith, G.A.: Z. Phys. A - Atomic Nuclei **331**, 519 (1988)
5. Hofmann, P., Hartmann, F.J., Daniel, H., von Egidy, T., Kanert, W., Markiel, W., Plendl, H.S., Machner, H., Reipe, G., Protic, D., Ziock, K., Marshall, R., Reidy, J.J.: Nucl. Phys. **A512**, 669 (1990)
6. McGaughey, P.L., Bol, K.D., Clover, M.R., DeVries, R.M., DiGiacomo, N.J., Kapustinsky, J.S., Sondheim, W.E., Smith, G.R., Sunier, J.W., Yariv, Y., Buenerd, M., Chauvin, J., Lebrun, D., Martin, P., Dousse, J.C.: Phys. Rev. Lett. **56**, 2156 (1986)
7. Balestra, F., Bossolasco, S., Bussa, M.P., Busso, L., Ferrero, L., Panzieri, D., Piragino, G., Tosello, F., Barbieri, R., Bendifioli, G., Rotondi, A., Salvini, P., Zenoni, A., Batusov, Yu.A., Falomkin, I.V., Pontecorvo, G.B., Sapozhnikov, M.G., Tretyak, V.I., Guaraldo, C., Maggiora, A., Rizzini, E.L., Haatuft, A., Halsteinslid, A., Myklebost, K., Olsen, J.M., Breivik, F.O., Jacobsen, T., Sørensen, S.O.: Nucl. Phys. **A491**, 541 (1989)
8. Riedlberger, J., Amsler, C., Doser, M., Straumann, U., Truöl, P., Bailey, D., Barlag, S., Gastaldi, U., Landua, R., Sabev, C., Duch, K.D., Heel, M., Kalinowsky, H., Kayser, F., Klempt, E., May, B., Schreiber, O., Weidenauer, P., Ziegler, M., Dahme, W., Feld-Dahme, F., Schaefer, U., Wodrich, W.R., Ahmad, S., Bizot, J.C., Delcourt, B., Jeanjean, J., Nguyen, H., Prevot, N., Auld, E.G., Axen, D.A., Erdman, K.L., Howard, B., Howard, R., White, B.L., Comyn, M., Beer, G., Marshall, G.M., Robertson, L.P., Botlo, M., Laa, C., Vonach, H.: Phys. Rev. **C40**, 2717 (1989)
9. Clover, M.R., DeVries, R.M., DiGiacomo, N.J., Yariv, Y.: Phys. Rev. **C26**, 2138 (1982)
10. Iljinov, A.S., Nazaruk, V.I., Chigrinov, S.E.: Nucl. Phys. **A382**, 378 (1982)
11. Cahay, M., Cugnon, J., Vandermeullen, J.: Nucl. Phys. **A393**, 237 (1983)
12. Hernandez, E., Oset, E.: Nucl. Phys. **A493**, 453 (1989)
13. Smith, G.A.: The elementary structure of matter. Richard, J.-M., Aslanides, E., Boccarda, N. (eds.), pp. 197, 219. In: Springer Proceedings in Physics, vol. 26. Berlin, Heidelberg, New York: Springer 1988
14. Bizzarri, R., Ciapetti, G., Dore, U., Fowler, E.C., Guidoni, P., Laakso, I., Marzano, F., Moneti, G.C., Zanello, D.: Nuovo Cimento **2**, 431 (1969)
15. Cugnon, J., Deneye, J., Vandermeullen, J.: Nucl. Phys. **A517**, 533 (1990)
16. Spencer, D., Edwards, D.N.: Nucl. Phys. **B19**, 501 (1970)
17. Armstrong, T., Chu, C., Clement, J., Elinon, C., Furic, M., Hartmann, K., Hicks, A., Hungerford, E., Kishimoto, T., Kruk, J., Lewis, R., Lowenstein, D., Lochstet, W., Mayes, B., Moss, R., Mutchler, G.S., Pinsky, L., Smith, G.A., Tang, L., von Witsch, W., Xue, Y.: Phys. Rev. **D36**, 659 (1987)
18. Davies, H., Muirhead, H., Woulds, J.N.: Nucl. Phys. **78**, 673 (1966)
19. Deutschmann, M., Honecker, R., Kirk, H., Klein, M., Nahnhauer, R., Hartmann, R., Plothow, H., Coccone, V.T., Counihan, M.J., Humble, S., Kellner, G., Morrison, D.R.O., Schmid, P., Stroynowski, R., Aniola, L., Coghen, T., Dziuniowska, K., Figiel, J., Zalewska, A., Leitner, E., Stiewe, J., Krolikowski, J., Para, A., Wroblewski, A.K.: CERN/EP/Phys. **78-1** (1978)
20. Sibertsev, A.A.: Nucl. Phys. **B** (1991) (submitted)
21. Yariv, Y., Fraenkel, Z.: Phys. Rev. **C20**, 2227 (1979)
22. Yariv, Y., Fraenkel, Z.: Phys. Rev. **C24**, 488 (1981)
23. Prael, R.E., Lichtenstein, H.: The User Guide to LCS: the LAHET Code System, LA-UR-89-3014 (1989)
24. Ghesquiere, G.: Proceedings of the Fourth International Symposium on $N\bar{N}$ Interactions. Syracuse University, New York 1975
25. Orfanidis, S.J., Rittenberg, V.: Nucl. Phys. **B59**, 570 (1973)
26. Roy, J.: Proceedings of the Fourth International Symposium on $N\bar{N}$ Interactions. Syracuse University, New York 1975, p. III-1
27. Jasselette, P., Cugnon, J., Vandermeullen, J.: Nucl. Phys. **A484**, 542 (1988)
28. Angelopoulos, A., Apostolakis, A., Armstrong, T.A., Bassalleck, B., Bueche, G., Fero, M., Gee, M., Graf, N., Koch, H., Lewis, R.A., Mandelkern, M., Minor, E., Poth, H., Rozaki, H., Sakellou, L., Schultz, J., Schwertel, J., Smith, G.A., Souliere, M.J., Usher, T., Wolfe, D.M.: Phys. Lett. **B212**, 129 (1988)
29. Bhaduri, R.K., Preston, M.A.: Structure of the nucleus. Reading, Mass.: Addison-Wesley 1975
30. Vandermeullen, J.: Nuovo. Cim. **28**, 60 (1980)
31. Hernandez, E., Oset, E.: Private communication
32. Bertsch, G., Scholten, O.: Phys. Rev. **C25**, 804 (1982)
33. CERN Program Library Section: The CERN Program Library, Geneva
34. Roberson, P., King, T., Kunselman, R., Miller, J., Powers, R.J., Barnes, P.D., Eisenstein, R.A., Sutton, R.B., Lam, W.C., Cox, C.R., Eckhouse, M., Kane, J.R., Rushton, A.M., Vulcan, W.F., Welsh, R.E.: Phys. Rev. **C16**, 1945 (1977)

FISSION OF HEAVY HYPERNUCLEI FORMED IN ANTIPIRON ANNIHILATION

T.A. Armstrong ¹, J.P. Bocquet ², G. Ericsson ³, T. Johansson ³, T. Krogulski ⁴ * ,
R.A. Lewis ¹, F. Malek ² † , M. Maurel ⁵, E. Monnand ⁵, J. Mougey ⁶, H. Nifenecker ²,
J. Passaneau ¹, P. Perrin ⁵, S.M. Polikanov ⁷, M. Rey-Campagnolle ⁸ ‡ , C. Ristori ⁵,
G.A. Smith ¹ and G. Tibell ³

¹Pennsylvania State University, University Park, PA 16802 USA.

²Institut des Sciences Nucléaires, Institut National de Physique Nucléaire et de Physique des Particles/Centre National de la Recherche Scientifique and University of Grenoble, France.

³Department of Radiation Sciences, Uppsala University, P.O. Box 535, S-75121 Uppsala, Sweden.

⁴Warsaw University, Bialystok Branch, PL-15-424 Bialystok, Poland.

⁵DRFMC, Centre d'Etudes Nucléaires de Grenoble, Boîte Postale 85X, 38041 Grenoble, France.

⁶Continuous Electron Beam Accelerator Facility, Newport News, VA 23606 USA.

⁷Gesellschaft für Schwerionenforschung Darmstadt, Postfach 110541, D-6100 Darmstadt, Germany.

⁸Centre de Spectrométrie Nucléaire et de Spectrométrie de Masse, Institut National de Physique Nucléaire et de Physique des Particles/Centre National de la Recherche Scientifique, F-91405 Orsay, France.

*Present address: Gesellschaft für Schwerionenforschung Darmstadt, Postfach 110541, D-6100 Darmstadt, Germany.

†Present address: Institut de Physique, Institut National de Physique Nucléaire et de Physique des Particles/Centre National de la Recherche Scientifique and the University of Lyon, France.

‡Present address: CERN/PPE, CH-1211 Genève, Switzerland.

Abstract

Heavy hypernuclei are produced in the annihilation of antiprotons in ^{238}U . The delayed fission of heavy hypernuclei and hypernuclei of fission fragments are observed by using the recoil-distance method. The lifetime of hypernuclei in the region of uranium is found to be $(1.25 \pm 0.15) \times 10^{-10}$ sec. It is observed that Λ hyperons predominantly stick to the heavier fission fragments. The yield of hypernuclei is found to be $(7.4 \pm 1.7) \times 10^{-3}$ per stopped antiproton. No coincidences with K^+ were found. Statistical and systematic errors on the number of events expected do not rule out this possibility.

PACS number(s): 21.80.+f, 25.85.-w, 27.90.+b

(Submitted to Phys. Rev. C)

1 INTRODUCTION

In previous papers we reported results of a search for heavy hypernuclei produced in the annihilation of antiprotons in ^{238}U [1] and ^{209}Bi [2]. The underlying idea of the experiment was that the non-mesonic decay of the Λ hyperon in a heavy hypernucleus leads to an excitation of the residual nucleus to an energy sufficient to induce fission. Thus, the decay of heavy hypernuclei would be observed as delayed fission with the lifetime of the hypernucleus.

The Λ hyperon can be produced in a secondary interaction of K mesons after $\bar{p}N$ annihilation with residual nuclei. More exotic reactions, such as the direct production of Λ hyperons on pairs of nucleons are also possible [3].

The annihilation of antiprotons in nuclei is accompanied by the emission of mesons and nucleons, giving the residual nucleus a rather high recoil momentum. This makes it possible to employ, in the study of heavy hypernuclei, the recoil-distance technique, earlier used in studies of short-lived fission isomers [4]. The characteristic feature of this technique is the experimental geometry which provides a strong suppression of prompt fission fragments, with a detection efficiency for delayed fission of about 1%.

The delayed fission lifetimes observed in the annihilation of antiprotons in ^{238}U and ^{209}Bi were found to be $(0.1^{+0.1}_{-0.05})$ ns [1] and $(0.25^{+0.25}_{-0.10})$ ns [2], respectively. It was assumed that the lifetimes measured are related to groups of nuclides in the vicinity of U and Bi, respectively.

As seen from the accuracy of the quoted results, it was impossible to conclude whether the probability of non-mesonic decay for these two groups of nuclei is the same or not. The shorter lifetime in the case of uranium may result from the fact that the recoil-distance

technique, although providing separation of delayed and prompt fission, does not exclude completely the recording of hypernuclei of fission fragments which are produced in the prompt fission of excited hypernuclei. Because of the high fissility of nuclei in the uranium region, the number of detected hypernuclei of fission fragments can be rather large. As will be discussed below this may result in too short a lifetime for delayed fission for the ^{238}U target.

Here we report results obtained with an improved experimental apparatus. It allowed us to impose additional criteria for the separation of prompt-fission events and thus made it possible to separate the delayed fission, caused by the decay of the Λ hyperon, from the hypernuclei of fission fragments. This was achieved by using the fact that fission fragments cause the emission of a large number of secondary electrons when they leave the target surface [5]. In contrast, when a slow heavy recoil is knocked out of the target, the number of secondary electrons is small.

The data on hypernuclei of fission fragments can be used in the analysis of the prompt fission of excited hypernuclei. We can understand the appearance of hypernuclei of fission fragments by using rather simple assumptions concerning the non-mesonic decay of a Λ hyperon. The possibility of explaining two different types of events using the same assumption on the non-mesonic decay of hypernuclei would be an additional argument in favour of the hypernuclear nature of the observed effect.

Furthermore, a detector was implemented to record K^+ mesons in coincidence with fission fragments. The observation of kaons in coincidence with events identified as the prompt or delayed fission of hypernuclei would be a direct confirmation of this identification.

In section 1 the experimental setup is described. In section 2 the experimental results

are presented. In section 3 we present the results of the data analysis performed on the assumption that the effect observed is related to the decay of hypernuclei, and in section 4 the results obtained are discussed.

2 EXPERIMENTAL SETUP

2.1 Principle and general description

Fig. 1a shows schematically how delayed-fission fragments are recorded by the recoil-distance method. In the case of prompt fission which occurs inside the target, the fission fragments cannot hit that part of the detector which is shadowed by the target backing (the hatched part). The delayed fission occurs in vacuum, at a certain distance from the target plane. This distance is determined by the velocity and lifetime of the recoiling nucleus. In this case the fragments can hit the shadowed area of the detector. Thus, the signature of delayed fission would be that a fission fragment is recorded in this part of the detector.

In principle, the scheme shown in Fig. 1a provides reliable suppression of the prompt-fission fragments at a level of at least 10^{-6} . However, the situation turns out to be somewhat different when it is used in the study of hypernuclei. There, in addition to hypernuclei of heavy elements there are also hypernuclei of fission fragments produced as the result of the prompt fission of excited hypernuclei. Since the hypernuclei of fission fragments are emitted from the target, they cannot hit the shadowed area of the detector. However this is true only if we ignore the decay of the Λ hyperon in a moving fragment.

Because of the relatively high velocity of fission fragments (about 10^{10} mm/s) the mean distance the fragments travel before the Λ hyperon decays is about 2 mm, comparable to the

size of the target. Since in the region of the fission-fragment masses the non-mesonic decay predominates, we may expect that in this decay the fission fragment receives a momentum which cannot be neglected. In a non-mesonic decay on a free nucleon the nucleons produced would have momenta of $400 \text{ MeV}/c$. When this decay occurs inside the nucleus, the Fermi motion of nucleons, as well as the rescattering of the nucleons produced, should be taken into account. It is then plausible to expect that the distribution of the momentum transfer to the fragments is broad and extends to several hundreds of MeV/c . Consequently, although the momentum transfer from the Λ decay is appreciably lower than the momentum of a fission fragment (about $4000 \text{ MeV}/c$), it is still sufficiently high to deflect the initial trajectory of the fragment. As a result, some fragments could hit the shadowed area of the detector near the target plane (Fig. 1b).

To distinguish between the delayed fission of heavy hypernuclei and the decay of hypernuclei of fission fragments, we made use of the following fact: while the delayed fission of heavy hypernuclei occurs in vacuum, the hypernuclei of prompt fission fragments are emitted from the target. In the latter case some tens of slow secondary electrons are emitted as a result of the interaction of the fragments with the surface layer of the target. A slow recoiling nucleus leaves the target with appreciably lower velocity than fission fragments and will thus produce fewer secondary electrons. Therefore, by measuring the number of low energy secondary electrons one can distinguish between these types of events. This was done using an electron detector placed in front of the target and operating in coincidence with the fission-fragment detectors. Those fragments which were recorded in the shadowed area of the detectors and accompanied by the emission of a large number of electrons were at-

tributed to the hypernuclei of fission fragments, and the rest of the shadow events attributed to delayed fission. The threshold of the electron detector could be set to such a low level that practically all delayed fission events were accompanied by a small but measurable signal from the detector.

In Fig. 2 we show the scheme of the whole experimental setup. The antiproton beam passed successively through the 0.1 mm Be window of the beam tube, a $3 \times 7 \text{ mm}^2$ slit in a scintillator used as an active collimator and through a variable mylar degrader. It was further slowed down in the plastic scintillator which served both as target backing and beam detector. Some antiprotons were stopped in the U target deposited on this scintillator, where they were captured to form antiprotonic atoms of uranium. The subsequent annihilation of antiprotons can induce many different processes. Some of these may lead to the formation of hypernuclei of residual excited nuclei which either undergo prompt or – after the emission of neutrons and mesons – delayed fission. In both cases the fission fragments are detected in coincidence by a pair of parallel plate avalanche counters (PPACs) placed perpendicularly to the target plane at a distance of 270 mm. The electron detector was positioned in front of the target at a distance of about 5 mm. The front face of the kaon detector was at 45 cm from the target, behind one of the PPACs subtending 16 % of the full solid angle.

2.2 Fission-fragment detectors

The two PPACs – $190 \times 290 \text{ mm}^2$ each – consisted of two planes of horizontal and vertical wires placed between two outer cathode planes and one central anode plane. They were filled with isobutane at a pressure of 7 Torr, and separated from the volume of the reaction chamber by 2 μm thick Mylar foils. The position resolution of the chambers along the beam

direction and in the perpendicular direction was found to be 1.0 and 1.8 mm, respectively. In addition, recording independently fast anode pulses, we obtained a timing signal needed for time-of-flight (TOF) measurements and the amplitude of anode pulses and thus the specific ionization of the detected particles. Combining these data for each event, it was possible to discriminate fission fragments from any background due to light particles from \bar{p} annihilation.

2.3 Target arrangement

The ^{238}U target was deposited, by ion implantation, on a 0.2 mm thick plastic scintillator backing, as a spot $2 \times 5 \text{ mm}^2$ of 0.2 mg/cm^2 thickness. The target surface was flat within $1 \mu\text{m}$. Backings with two different widths, 2.5 and 8.0 mm, were used. The scintillator provided the zero-time signal required in the TOF measurement. An additional adjustable degrader, placed before the scintillator, optimized the stopping rate of antiprotons in the uranium target.

2.4 Secondary-electron detector

A microchannel plate electron multiplier (MCP) was used to detect secondary electrons produced in the interaction of fission fragments and recoil nuclei with the target. The electrons were accelerated and focused by an electric field of 5 kV between the target and the entrance of the MCP detector. Microchannel detectors demand a vacuum of 10^{-7} Torr to perform in a stable way. The leakage of isobutane through the windows of the fission counters did not permit such a vacuum in the whole volume of the reaction chamber. It could be sustained locally around the target and MCP by an additionnal cryogenic pump. Nevertheless, in the course of the experiment, the MCP detector had to be replaced to ensure

a proper response.

2.5 K^+ meson detector

In the present experiment a kaon range telescope (KRT) was also used. A detailed description of the KRT is given in ref. [6]. It is a rectangular parallelepiped $100 \times 100 \times 50 \text{ cm}^3$, composed of 100 cells constructed with alternating plates of copper and acrylic scintillator. It provides coarse tracking in three dimensions as well as energy loss and timing information. Both the scintillator and the copper serve as moderators, contributing roughly equally to the energy loss. The stopped K^+ mesons decay in the KRT ($K^+ \rightarrow \mu^+ \nu$ or $\pi^+ \pi^0$) with a mean life of 12 ns. The signals from the cells are identified in two groups, the first one corresponding to the stopped K meson and the second one to the pion or muon from its decay. The momentum range of the detected kaons was $250 < P_k < 750 \text{ MeV}/c$, the upper limit being determined by the thickness of the KRT, and the lower limit by attenuation in material between the target and the KRT.

3 EXPERIMENTAL RESULTS

The experiment was carried out at the CERN Low Energy Antiproton Ring, LEAR, using a \bar{p} beam with $105 \text{ MeV}/c$ momentum. A total of 2.5×10^{10} and 1.6×10^{10} antiprotons were delivered on the ^{238}U targets deposited on 2.5 and 8 mm wide scintillators, respectively. As a result, 1128 'shadow events' with one fragment detected in the shadowed zone of the PPACs and the complementary fragment in the non-shadowed area were recorded in the first case and 350 in the second case. It should be noted that, compared to the previous measurements [1, 2], there was an appreciable number (139) of double-hit events, with two

fission fragments detected in the shadowed area. Only about one percent of the antiprotons are stopped in the target material. With the present geometry of the experiment (Fig. 2), a significant fraction of the antiprotons are stopped in the MCP detector holder whose front end is viewed by the shadowed area of the PPACs. The double-hit events may arise from antiproton induced prompt fission of impurities on this front end. This assumption agrees with the result of an additional experiment with a 2.5 mm wide scintillator without target material. Here, four double-hit events were registered with 2×10^9 incoming antiprotons.

A data-acquisition system based on CAMAC operating under a NORD computer control was used to record the data. A registered event consisted of the space-time coordinates of the incident hits in the PPACs and KRT, the amplitude of the corresponding analogue pulses as well as the amplitude and timing signals from the MCP detector. The MCP and PPACs were calibrated with a ^{252}Cf source in 4π geometry.

Fig. 3 shows the two-dimensional distributions dE/dx vs TOF obtained from the PPACs with the U target (deposited on the 2.5 mm wide scintillator) irradiated with antiprotons. Here (a) corresponds to events with both fragments registered in the non-shadowed area of the PPACs (prompt fission) and (b) to events with one fragment detected in the shadowed part. The results for both types of events are consistent with the calibration data from the fission fragments of ^{252}Cf . In Fig. 4 the corresponding pulse-height distributions obtained from the MCP detector are presented. Fig. 5 shows the two-dimensional TOF spectrum of fission fragments for prompt fission (a) and shadow events (b). Both cases correspond to symmetric fission. Fig. 5a shows that even for prompt fission, where the counting rate was relatively high, the contribution from random coincidences was negligible.

A comparison of the pulse-height distributions of signals from the MCP detector, for prompt fission (Fig. 4a) and for the shadow events (Fig. 4b), shows that for prompt fission there is one broad peak. This peak is located in the same region as the one obtained in the ^{252}Cf calibration. The shadow events, however, are divided into two groups. One of them is centered around channel 1000 and the other group is located below channel 250. We attribute the first group to prompt fission of excited hypernuclei, i.e., to those cases when one of the fragments, as a result of the Λ -hyperon decay, is deflected into the shadowed area of the PPAC. The second group is assumed to be due to fission events resulting from the decay of heavy hypernuclei.

The main conclusions drawn from the experimental distributions in Figs. 3-5, are the following:

- i) there are two types of shadow events, one due to the hypernuclei of fission fragments and the other to delayed fission of heavy hypernuclei;
- ii) the fission is symmetric both for prompt and delayed events.

In the following we perform an analysis of our results based on these conclusions. The experimental coordinate distributions for fission fragments are compared with those obtained in a Monte Carlo simulation to be described later. In order to simplify the discussion, we confine ourselves to the distributions in the coordinate along the axis, here denoted by X , which is directed perpendicular to the target plane with positive and negative values of X downstream and upstream of the target, respectively (Fig. 1). This is the coordinate for which the dependence of the shadow effect upon the characteristics of the non-mesonic decay (lifetime and momentum transfer) is seen in the most transparent way. In fact, the coordinate

distributions along the axis parallel to the target plane, should depend only weakly on the lifetime of hypernuclei and the momentum transfer in the Λ decay.

In Fig. 6 we show the experimental X coordinate distributions of shadow events accompanied by a small or large number of secondary electrons. We attribute these two distributions to the delayed fission of heavy hypernuclei and to hypernuclei of fission fragments, respectively. They are clearly different both in the shadowed and non-shadowed areas of the detector. The events corresponding to hypernuclei of fission fragments are localized closer to the target plane, and their coordinate distribution in the shadowed area is steeper.

During the experiment K^+ mesons were registered in coincidence with fission fragments. Thus, 436 K^+ mesons were observed in coincidence with 1.25×10^6 prompt fission events. No coincidences were observed with the shadow events.

4 DATA ANALYSIS

4.1 Prompt fission

The sample of events with two fragments detected in coincidence in the non-shadowed area of the PPACs is mainly due to prompt fission induced by stopped antiprotons. It also contains a small admixture ($\sim 10^{-3}$) of events from prompt and delayed fission of hypernuclei which can be neglected at this stage of analysis. The prompt fission is a result of antiproton annihilation through many channels, in which the residual nucleus is excited to an energy above the fission barrier. Here, the antiproton induced fission will not be analysed in detail; it has been studied independently [7] showing a symmetric mass distribution of fission fragments which is centered at $M = 106u$ with a dispersion $\sigma(M) = 22u$. Only those characteristics

which help to better describe the production of hypernuclei will be investigated here.

In the case of prompt fission both fragments hit the PPACs in the non-shadowed zone. The X position distribution is in this case determined by the momentum distribution of excited nuclei produced in the annihilation, the geometry of the PPACs, and the energy loss of the fragments in the target. In Fig. 7 the solid line shows the X -position distribution of the prompt-fission events measured in the experiment. The rather strong decrease in the distribution near the target plane reflects the absorption in the target and the PPAC windows. The slope of the distribution at large distances from the target plane is due to the decreasing contribution of high momentum recoils. These effects were taken into account by using a geometrical detection efficiency determined from the X distribution measured for single fission fragments.

In the same phenomenological approach as used previously [1, 2], the isotropic momentum distribution of fissioning nuclei was approximated by the function:

$$N(p) = p^{n/2} \exp(-p/p_0) \quad (1)$$

where p_0 and n are free parameters. In fact, there is a third non-explicit parameter involved, namely a cutoff, p_{max} , for acceptable values of the momentum of the fissioning nucleus. The dashed line in Fig. 7 is the result of the simulation obtained with the parameter values of $n = 2$, $p_0 = 400$ MeV/c, $p_{max} = 2000$ MeV/c. Using the number of fission fragments recorded, their detection efficiency in the PPACs (see Sec. 3.4), and the corresponding number of \bar{p} stopped in the U target, it is possible to calculate the probability of prompt fission of ^{238}U induced by stopped antiprotons. This probability was found to be $(85 \pm 15)\%$ which agrees with the estimate of [8].

4.2 Hypernuclei of fission fragments

The analysis of the hypernuclei of fission fragments, i.e., of shadow events accompanied by the emission of a large number of secondary electrons, is based on the model discussed in section 1.1.

As a first stage of the process we consider the antiproton annihilation which leads to the production of an excited hypernucleus. The momentum distribution of these hypernuclei is assumed to be isotropic and given by the expression in Eq. 1. This is a purely phenomenological approach, in which we neglect details of the various processes governing the momentum distribution of the hypernuclei.

The second step of this process is the prompt fission of the excited hypernucleus. One of the fragments produced carries the Λ hyperon which undergoes non-mesonic decay $\Lambda + N \rightarrow N + N$. The lifetime for this decay is assumed to be 2.5×10^{-10} s, i.e., close to the free Λ lifetime.

When an excited hypernucleus undergoes fission, the Λ hyperon sticks to one of the fission fragments. The probability of the Λ sticking can be a function of the fission-fragment mass.

It is clear that the Λ particle must have been initially attached to the fragment detected in the shadowed region. The mass of this fragment relative to that of the original fissioning hypernucleus can be determined by means of the double velocity technique. This technique is based upon the fact that nucleon evaporation from the fragments after fission has forward-backward symmetry in the fragment frame, and, therefore, does not change the fragment velocity on the average. If 1 and 2 label the fission fragments, momentum conservation at

the time of fission gives the following relation between masses and velocities:

$$M_1/(M_1 + M_2) = V_2/(V_1 + V_2) \quad (2)$$

This relation added to the conservation of velocities on the average, provides the ratio $R_1 = M_1/(M_1 + M_2)$ from the measurement of the velocities of the two fragments. Here it is sufficient to have the velocities in relative units (see also Sec. 3.3). The attachment probability of the Λ particle to a fragment of mass M_1 , $A_\Lambda(R_1)$, can be expressed in terms of the counting rate $N_{F\Lambda}(R_1)$ of fission fragments observed in the shadowed region in coincidence with a complementary fragment in the non-shadowed region, with a high MCP signal, and a corresponding mass ratio R_1 (see appendix).

Fig. 8a gives the variation of the experimental ratio $N_{F\Lambda}(R_1)/(N_{F\Lambda}(R_1) + N_{F\Lambda}(R_2))$ (dashed line) as a function of R_1 , and of the same ratio corrected for the fragment mass resolution and for the difference in detection efficiency between light and heavy fragments (solid line). The last one shows the variation of the attachment probability of the Λ particle to the fragment of mass M_1 . A clear positive correlation is observed implying that high mass fragments are detected in a greater number in the shadowed region than are low mass fragments. The correlation observed in Fig. 8a for the corrected histogram can be described by the relation:

$$A_\Lambda(R) = 0.5 + 1.7(R - 0.5) \quad (3)$$

Fig. 8b is the same as Fig. 8a but for delayed hypernucleus fission (low MCP amplitudes). No apparent correlation between the two ratios is found. This was expected since, in the case of the decay of heavy hypernuclei outside the target, no preference should exist for a

light or a heavy fragment to be detected in the shadowed region.

While the data on the TOF (velocity) of fragments in the shadow events provide information on the Λ -hyperon attachment to fission fragments, the X distribution can be used to obtain information on the momentum transfer in the non-mesonic Λ -hyperon decay. In the analysis of this distribution we assume that the probability of the Λ -hyperon attachment is proportional to the fragment mass. The calculation of the deflection of the fragments to the shadowed area involves only the momenta of the fragments, which in binary fission are the same for heavy and light fragments. Therefore, the results of the calculation of the momentum transfer in the Λ -hyperon decay depends very little on the assumption about the Λ -hyperon sticking to fragments. The mass distribution of fission fragments quoted in the previous section was used. We neglect details of the interaction of the two nucleons produced in the non-mesonic decay, and assume that the distribution of the momentum transfer k to the fragment is described by the function:

$$N(k) = k/(1 + \exp((k - k_0)/\Delta k)) \quad (4)$$

where k_0 and Δk are free parameters. The low-momentum part of the distribution corresponds to those cases when both nucleons either transfer all their energy to the residual nucleus or are emitted without interacting with the residual nucleus. The high momentum part of the distribution includes those events, when the high momentum tail of the nucleon momentum distribution is involved or when the energy released in the non-mesonic decay is carried away by an alpha particle or a heavier fragment.

In Figs. 9a and 9b the solid lines show the experimental distribution of the X coordinate of both fragments and of the quantity $(X_{sh} + X_{nsh})$, respectively, where X_{sh} and X_{nsh} are

the X coordinates in the shadowed and non-shadowed areas of the PPACs. The latter distribution is related to the projection of the recoil momentum on the X axis. The dashed histograms in Figs. 9a and 9b are best fits from the Monte Carlo calculations corresponding to $k_0 = 350$ MeV/c and to $\Delta k = 150$ MeV/c. The p_0 was found to be equal to 450 MeV/c. The cutoff values for the momentum transfer in the \bar{p} annihilation and in the non-mesonic hyperon decay were 2000 and 1000 MeV/c, respectively. Lower cutoff values do not give a good description of the experimental data. It was also checked that these results show a very weak dependence on the lifetime of hypernuclei of fission fragments.

4.3 Delayed fission

The aim of the analysis of the data on delayed fission was to estimate the lifetime of hypernuclei undergoing non-mesonic Λ -hyperon decay. Here we used the fact that only the position distribution in the X coordinate, perpendicular to the target plane, is sensitive to the lifetime. The analysis of this distribution for delayed fission was carried out assuming that it is entirely determined by the lifetime of hypernuclei and their momentum distribution. Consequently, in the Monte Carlo simulation we generated only the projection of the momentum perpendicular to the target plane. In so doing we employ a phenomenological approach, ignoring all details related to the production and scattering of hypernuclei in the target.

The Monte Carlo simulation of the delayed fission of heavy hypernuclei showed that in a broad range of lifetimes the X distribution in the shadow region remains steep at any distance from the target plane. The flat part of the experimental distribution in the shadowed area (see Fig. 6) may include the above discussed background events due to the prompt fission of

impurities on the MCP-detector holder (see Sec. 2). This background could be excluded in the analysis on the basis of the arguments discussed in the following.

In the case of delayed fission of hypernuclei, coincidences of fragments are only recorded when the projection of the nuclear recoil on the X axis is positive, i.e., the momentum is directed downstream of the target. On the other hand, fragments resulting from the prompt fission of impurities on the MCP are detected (in coincidence) only if the momentum transferred to the fissioning nucleus is directed upstream of the target. As a result the quantity $(X_{sh} + X_{nsh})$ should be negative for the background while it is mainly positive for good events. It can be negative, sometimes, due to the kinematics of the Λ decay. However, the fraction of these events, as follows from a Monte Carlo simulation is small.

In Fig. 10a we show the measured X distribution of the shadow events with low-amplitude signals from the MCP detector (solid line) constructed with the condition $(X_{sh} + X_{nsh}) > 0$ imposed. We can see that after imposing this cut the distribution becomes steeper than the initial one (Fig. 6). In Fig. 10b we show the measured $(X_{sh} + X_{nsh})$ distribution.

In our Monte Carlo calculation we assumed that the momentum distribution of the recoils has the form given in Eq. 1. The cutoff parameter, p_{max} , was 1200 MeV/c. The analysis has shown that for lower values of this cutoff, we cannot satisfactorily describe the experimental position distribution.

The parameter values which correspond to the best description of the experimental X distribution are $\tau = (1.25 \pm 0.15) \times 10^{-10}$ s and $p_0 = (350 \pm 50)$ MeV/c. This value of the lifetime ($\chi^2 = 15.7$ for 13 degrees of freedom) was found to be very little dependent on the

value of p_0 . In Fig. 10a the dashed line shows the X distribution calculated with the imposed condition $(X_{sh} + X_{nsh}) > 0$. The distribution $(X_{sh} + X_{nsh})$ calculated with these parameters reproduces well the data with $(X_{sh} + X_{nsh}) > 0$ (Fig. 10b).

To check the result on the hypernucleus lifetime, another procedure of calculation was used. This procedure was applied both to the present data for uranium and to the previously registered data for bismuth [2]. The range of a heavy nucleus can be written as:

$$\vec{r} = \vec{V}_{recoil} \times \tau \quad (5)$$

where \vec{V}_{recoil} is the recoil velocity, and τ the lifetime. This does not require any knowledge of the recoil momentum distribution and gives the mean value of the lifetime if one knows the mean recoil velocity and the mean range. The recoil velocity and the lifetime are uncorrelated. Projecting on the beam axis X one obtains for the mean lifetime:

$$\langle \tau \rangle = \frac{\langle r_X \rangle}{\langle (\vec{V}_{recoil})_X \rangle} \quad (6)$$

The experimental position distribution in the shadowed region is well reproduced if the range distribution r_X is taken as an exponential.

The mean recoil velocity is given by

$$\langle \vec{V}_{recoil} \rangle = \frac{1}{2} \langle \vec{V}_1^{lab} + \vec{V}_2^{lab} \rangle. \quad (7)$$

where \vec{V}_1^{lab} and \vec{V}_2^{lab} are the velocities of the two fission fragments in the laboratory system.

The projection of the recoil velocity on the beam axis X is :

$$\langle (\vec{V}_{recoil})_X \rangle = \frac{1}{2} \langle |\vec{V}_1^{lab}| \cos \theta_1 + |\vec{V}_2^{lab}| \cos \theta_2 \rangle \quad (8)$$

where $\theta_{1,2}$ are the angles between the fragment trajectories and the beam axis. The measured velocity spectra of fission fragments were calibrated by using the mean velocity of fragments in the laboratory system, (1.2 ± 0.1) cm/ns [9]. Fig. 11 shows the calculated distribution of the recoil velocity projection. Table 1 summarizes the mean values of the range, recoil velocity, and corresponding lifetimes for hypernuclei in the regions of Bi and U.

We can see that the lifetime for U quoted in Table 1 agrees well with that obtained in the Monte Carlo simulation. The lifetimes of Bi and U hypernuclei are smaller than the free Λ lifetime. In Fig. 12 we display the results for Bi and U together with the lifetimes of the free Λ hyperon and of ${}_{\Lambda}^{11}B$ and ${}_{\Lambda}^{12}C$ [10].

The position distribution of the shadow events detected with the target on a wide backing was measured without separating heavy hypernuclei from hypernuclei of fission fragments. The number of events of each type was estimated with a Monte Carlo calculation using the parameters obtained with the data from the narrow backing target. Their sum agrees within the statistical error with the number of events measured. This confirms our interpretation of the observed effects.

4.4 YIELDS

In order to estimate the yield of the processes studied here, it is necessary to know the efficiencies of detection for each process, and the number of antiprotons stopped in the target. The latter can be deduced from the fraction of the beam impinging on the target and from the stopping power of the target material.

The detection efficiency of single fragments from prompt fission was obtained in a Monte Carlo simulation which took into account the solid angle of the PPACs and the measured

decrease of the counting rate for the fragments emitted at a small angle with respect to the target plane. This decrease is due to absorption and multiple scattering of the fragments in the target. The detection efficiency, including solid angle, is 0.05 for each PPAC. It decreases to $(3.4 \pm 0.4) \times 10^{-3}$ when the fragments are measured in coincidences.

The detection efficiency of hypernuclei of fission fragments is determined by the same factors as that for prompt fission but is strongly reduced (20 times). This is due to the fact that only a small fraction of the fragments are deviated to the shadowed area of the PPACs, as a result of Λ decay. It was found to be $(1.7 \pm 0.2) \times 10^{-4}$.

The detection efficiency of delayed-fission fragments is essentially determined by the recoil-distance distribution of hypernuclei and was obtained from a Monte Carlo simulation equal to $(4.2 \pm 0.4) \times 10^{-3}$. It has to be corrected for the absorption of recoil nuclei in the target. This effect was estimated from a comparison of the yields of hypernuclei for two targets, 100 and 200 $\mu\text{g}/\text{cm}^2$ thick. We found that about 50 % of the recoils are stopped in the 200 $\mu\text{g}/\text{cm}^2$ thick target. Consequently the detection efficiency of heavy hypernuclei produced in this target was $(2.1 \pm 0.7) \times 10^{-3}$.

Table 2 gives the number of registered events N_{exp} , the detection efficiencies ε , the corresponding number of events produced in the target, N_{target} , and the calculated yields Y per stopped antiproton of the three processes: prompt fission (PF), and the delayed and prompt fission of hypernuclei, (DHF) and (PHF), respectively. The accuracy of the calculation of the yields of prompt and delayed hypernucleus fission is mainly determined by the error in the evaluation of the number of antiprotons passing through the target ($\sim 15\%$). In the case of heavy hypernuclei the main uncertainty ($\sim 30\%$) comes from the estimate of the number

of recoil hypernuclei absorbed in the target.

5 DISCUSSION

In the discussion of the results obtained, we first present those facts which support the hypernucleus-production hypothesis. They are the following:

- i) the deviation of the prompt-fission fragment from its initial trajectory towards the shadowed zone of the PPACs;
- ii) the predominant detection of heavy prompt-fission fragments in the shadowed area;
- iii) the symmetric mass distribution for delayed fission fragments.

As was shown in section 3.2, to explain the position and $(X_{sh} + X_{nsh})$ distributions for the prompt fission fragments which hit the shadowed zone of the PPACs, it is necessary to assume that a momentum up to a few hundred MeV/c is transferred to the fragment in flight. Such an effect can occur if a Λ hyperon decays with a lifetime of about 10^{-10} s and, as a result of this decay, neutrons or protons are emitted with momenta close to 400 MeV/c. The only other particles which can be emitted from a fission fragment with such a lifetime are photons but the momentum transfer in this case is too small (1-2 MeV/c) to explain the experimental observation.

The fact that predominantly heavy prompt-fission fragments are registered in the shad-

the selected shadow events and K^+ can be written:

$$N_{K^+} = N_{sh} \times f \times \varepsilon \quad (9)$$

where N_{sh} is the number of selected shadow events, f is the fraction of K^+ in the K mesons produced in association with the Λ particles and ε is the kaon detection efficiency.

The efficiency for identifying K^+ with the KRT in the momentum range 250 - 750 MeV/c was determined from the inclusive number of K^+ per annihilation measured in experiment PS183 [13] with a uranium target, and from the number of K^+ detected in coincidence with the prompt fission events. It was found to be $(1.1 \pm 0.2)\%$. With an estimated branching ratio of $f = K^+/(K^+ + K^0) = 0.43$ for annihilation on the uranium nucleus, we predict $N_{K^+} = 5$. It is unlikely that the error on this number is purely statistical, as its prediction is model-dependent and hence subject to systematic error.

For example, in making this prediction, no angular correlation were assumed. The recoil-distance method is more efficient for those nuclei with momenta directed perpendicular to the target plane. Therefore, we can expect from momentum conservation that kaons in coincidence with fission events are emitted preferentially in a direction perpendicular to the target plane. Since the KRT was located at 90° to the target plane, the expected number of kaon-delayed fission coincidences may be reduced by about a factor of two. Zero events were observed.

As was indicated in the previous section, it is possible to obtain a good description of the experimental data on the delayed fission with a cutoff of the momentum transfer in the \bar{p} annihilation at 1200 MeV/c. This value is in good agreement with the upper limit of the recoil momentum distribution calculated by Cugnon et al. [14]. Therefore, we assume that the

observed heavy hypernuclei are predominantly hypernuclei of uranium isotopes with masses slightly below 238, as found in Ref. [14]. On the other hand, in the case of hypernuclei of fission fragments, the required minimum cutoff value for the recoil momentum is 2000 MeV/c (see Sec. 3.2). This value is consistent with the fact that on the average 18 neutrons are emitted in the \bar{p} induced fission [7]. As a result the required cutoff for the momentum transfer in the case of heavy hypernuclei becomes higher.

From Table 2 we can see that the total hypernucleus-formation probability per stopped antiproton is about 7.4×10^{-3} . The yield of hypernuclei in the \bar{p} annihilation in uranium was estimated in Ref. [14] to be 9.7×10^{-3} , which is consistent with our present result. It can be compared with the measured Λ^0 production rate in complex nuclei given in Ref. [15] to be $(1.9 \pm 0.4)\%$ per stopped antiproton. From this, one may deduce that in \bar{p} annihilation on heavy nuclei:

- i) the Λ^0 production rate accounting for hypernuclear formation is $(2.6 \pm 0.5)\%$;
- ii) the probability of the Λ attachment to a heavy nucleus is about 25 %. This is very close to the value found in reactions with stopped K^- ($\sim 30\%$, Ref. [16]).

6 CONCLUSION

The main results of the present experiment are the following:

- i) the annihilation of antiprotons in ^{238}U leads to the production of hypernuclei of fission

fragments and of heavy hypernuclei in the region of uranium;

ii) the lifetime of the heavy hypernuclei is found to be $(1.25 \pm 0.15) \times 10^{-10}$ s;

iii) when the fission of an excited hypernucleus occurs, the Λ hyperon predominantly sticks to the heavy fragment; this fact can be used in the analysis of the dynamics of fission [17];

iv) the probability of Λ hyperon attachment to a heavy nucleus, following \bar{p} annihilation is estimated to be about 25%;

v) we do not find with significant confidence that K^+ are produced in coincidence with the hypernuclear events. However, this conclusion depends on complex and poorly known features of kaon production in heavy nuclei.

Acknowledgements

This experiment has benefitted from the high quality technical support from CERN. We express our gratitude in particular to N. Mezin and J. Place who carried out the mechanics and to the LEAR group for their continuous effort on beam settings. We are also indebted to B. Gay for his help in high vacuum matters. We thank N. Trautmann (Mainz Univ.) who prepared the Cf source, H. Folger (GSI) and D. Ledu (CSNSM-Orsay) who prepared

the targets. We acknowledge fruitful discussions with J. Cugnon and J. Vandermeulen. The Swedish participants (G.E., T.J. and G.T.) are indebted to the Swedish Natural Science Research Council for support. The US part of this work was supported by The Air Force Office of Scientific Research under grant 87-0246.

References

- [1] J.P. Bocquet, M. Epherre-Rey-Campagnolle, G. Ericsson, T. Johansson, J. Konijn, T. Krogulski, M. Maurel, E. Monnand, J. Mougey, H. Nifenecker, P. Perrin, S. Polikanov, C. Ristori and G. Tibell, *Phys. Lett.* B182 (1986) 146.
- [2] J.P. Bocquet, M. Epherre-Rey-Campagnolle, G. Ericsson, T. Johansson, J. Konijn, T. Krogulski, M. Maurel, E. Monnand, J. Mougey, H. Nifenecker, P. Perrin, S. Polikanov, C. Ristori and G. Tibell, *Phys. Lett.* B192 (1987) 312.
- [3] J. Cugnon and J. Vandermeulen, *Phys. Lett.* 146B (1984) 16 and *Ann. Phys. (France)* 14 (1989)49.
- [4] V. Metag, E. Liukkonen, G. Sletten, O. Glomset and S. Bjørnholm, *Nucl. Instrum. Methods* 114 (1974) 445.
- [5] H.G. Clerc, H.J. Gehrhardt, L. Richter and K.H. Schmidt, *Nucl. Instrum. Methods* 113 (1973) 325.
- [6] T.A. Armstrong, D.M. Elias, R.A. Lewis, E.D. Minor, J. Passaneau and G.A. Smith, *Nucl. Instrum. Methods* A289 (1990) 109.
- [7] J.P. Bocquet, F. Malek, H. Nifenecker, M. Rey-Campagnolle, M. Maurel, E. Monnand, P. Perrin, C. Ristori, G. Ericsson, T. Johansson, G. Tibell, S. Polikanov, T. Krogulski and J. Mougey, to be published in *Z. Phys.D* (1992) .
- [8] F. Malek, *Etude de la fission des hypernoyaux. Thèse Université Joseph Fourier, Grenoble*, 1990.ISN 90-86.

- [9] V.E. Viola Jr, Nucl. Data A1 (1966)391.
- [10] R. Grace, P.D. Barnes, R.A. Eisenstein, G.B. Franklin, C. Maher, R. Reider, J. Seydoux, S. Bart, R.E. Chrien, P. Pile, Y. Xu, R. Hackenburg, E. Hungerford, B. Bassalleck, M. Barlett, E.C. Milner and R.L. Stearns, Phys. Rev. Lett. 55 (1985) 1055.
- [11] B. Povh, Ann. Rev. Nucl. Part. Sci. 28 (1978) 1.
- [12] S. Bjørnholm and J.E. Lynn, Rev. Mod. Phys. 52 (1980) 25.
- [13] E.D. Minor, T.A. Armstrong, R. Bishop, V. Harris, R.A. Lewis and G.A. Smith, Z. Phys. A336 (1990) 461.
- [14] J. Cugnon, P. Deneye and J. Vandermeulen, Phys. Rev. C41 (1990) 1701.
- [15] G.T. Condo, T. Handler and H.O. Cohn, Phys. Rev. C29 (1984) 1531.
- [16] M. Csejthe-Barth, G. Schorochoff and P. Van Binst, Nucl. Phys. B14 (1969) 330.
- [17] H. Nifenecker and F. Malek, Nucl. Phys. A531 (1991) 539.

Appendix

The count rate $N_{F\Lambda}(R_1)$ of fission fragments observed in the shadowed region, in coincidence with a complementary fragment in the open region, a high amplitude MCP signal and a corresponding mass ratio R_1 can be written:

$$N_{F\Lambda}(R_1) = N_{HN} \times P_{pf} \times F(R_1) \times A_{\Lambda}(R_1) \times \eta_{MCP} \times \epsilon(R_1)$$

where:

N_{HN} is the production rate of hypernuclei;

P_{pf} is the probability that a hypernucleus undergoes prompt fission, the lambda remaining attached to one of the fragments;

$F(R_1)$ is the probability that the fragments of mass m_1 and m_2 are produced (obviously, $F(R_1) = F(R_2)$);

$A_{\Lambda}(R_1)$ is the attachment probability of the lambda particle to fragment of mass m_1 ;

η_{MCP} is the detection efficiency, very close to unity, of the secondary electron detector when two fission fragments emerge from the target;

$\epsilon(R_1)$ is the probability that one of the fission fragments is detected, after deflection due to the lambda decay, in the shadowed area and the other fragment in the open area of the parallel plate detector.

By definition $A_\Lambda(R_1) + A_\Lambda(R_2) = 1$. It follows that:

$$\mathcal{A}_{Exp}(R_1) = \frac{N_{F\Lambda}(R_1)}{N_{F\Lambda}(R_1) + N_{F\Lambda}(R_2)} = \frac{A_\Lambda(R_1) \epsilon(R_1)}{A_\Lambda(R_1) \epsilon(R_1) + A_\Lambda(R_2) \epsilon(R_2)}$$

and:

$$\mathcal{A}_{Cor}(R_1) = \frac{\frac{N_{F\Lambda}(R_1)}{\epsilon(R_1)}}{\frac{N_{F\Lambda}(R_1)}{\epsilon(R_1)} + \frac{N_{F\Lambda}(R_2)}{\epsilon(R_2)}} = A_\Lambda(R_1) .$$

where \mathcal{A}_{Exp} and \mathcal{A}_{Cor} are the experimental and efficiency corrected ratios.

Target	$\langle X \rangle$ mm	$\langle (V_{recoil})_X \rangle$ mm/ns	$\langle \tau \rangle$ ns
Bismuth	$0.14 \pm^{0.020}_{0.025}$	$0.79 \pm 0.05 (\pm 0.25)$	$0.18 \pm 0.04 (\pm 0.06)$
Uranium	$0.125 \pm^{0.019}_{0.015}$	$0.95 \pm 0.07 (\pm 0.23)$	$0.13 \pm 0.03 (\pm 0.03)$

Table 1: Results obtained using the 'mean' method both for the U (present data) and Bi (1986 data) targets. The systematical errors are given within parentheses.

	PF	PHF	DHF	PHF+DHF
N_{exp}	625 358	238	438	676
ϵ	$(3.4 \pm 0.4) 10^{-3}$	$(1.7 \pm 0.2) 10^{-4}$	$(2.1 \pm 0.7) 10^{-3}$	\times
N_{target}	$(1.84 \pm 0.22) 10^8$	$(14 \pm 2) 10^5$	$(21 \pm 7) 10^4$	$(16 \pm 3) 10^5$
Y	0.85 ± 0.15	$(6.5 \pm 1.3) 10^{-3}$	$(9.6 \pm 3.4) 10^{-4}$	$(7.4 \pm 1.7) 10^{-3}$

Table 2: The yields of prompt fission and hypernucleus formation in \bar{p} annihilation on ^{238}U .

Figure: 1 Schematic representation of the recoil-distance method as applied to the study of (a) delayed fission of heavy hypernuclei, (b) decay of hypernuclei of fission fragments. Both types of events can provide hits in the shadowed region (hatched) of the detectors while prompt fission cannot.

Figure: 2 Scheme of the experimental setup (not to scale).

Figure: 3 dE/dx versus TOF (time-of-flight between target backing scintillator and PPAC) measured with the PPACs for two types of events: (a) both fragments in coincidence are in the non-shadowed area, (b) one of the fragments is in the shadowed area.

Figure: 4 Amplitude spectrum given by the MCP for events with (a) both fragments in coincidence in the non-shadowed area, (b) one of the fragments in the shadowed area.

Figure: 5 Time-of-flight of one fragment versus time-of-flight of the other for events with (a) both fragments in coincidence in the non-shadowed area, (b) one of the fragments in the shadowed area.

Figure: 6 X -position distributions of coincident fragments in the PPACs for events with one fragment in the shadowed area. The solid and dashed lines represent the events accompanied by a low and high amplitude MCP signal, respectively.

Figure: 7 X -position distributions of the prompt fission fragments in the PPACs (solid line); the dashed line was obtained with the Monte Carlo simulation.

Figure: 8 Counting ratio $N_{F\Lambda}(R_1)/(N_{F\Lambda}(R_1) + N_{F\Lambda}(R_2))$ versus the ratio $R_1 = M_1/(M_1 + M_2)$ for the shadow events (dashed line). The solid line represents this ratio after efficiency correction for: (a) events with high amplitude MCP signal, (b) events with low amplitude MCP signal.

Figure: 9 Distributions for the fragments from prompt hypernucleus fission, (a) X -position in the PPACs, (b) $(X_{sh} + X_{nsh})$. The solid line corresponds to the experimental data and the dashed line is the result of the simulation.

Figure: 10 Distributions for the fragments from delayed hypernuclear fission, (a) X -position in the PPACs of the fragments with $(X_{sh} + X_{nsh}) > 0$, (b) $(X_{sh} + X_{nsh})$. The solid line corresponds to the experimental data and the dashed line is the result of the simulation.

Figure: 11 Distribution of the X-component of the recoil velocity as deduced from the measured fragment velocities.

Figure: 12 Lifetime of hypernuclei as a function of their mass. (^{12}C and ^{11}B data are from Ref. [10], ^{209}Bi and ^{238}U - this work.) Only statistical errors are given.

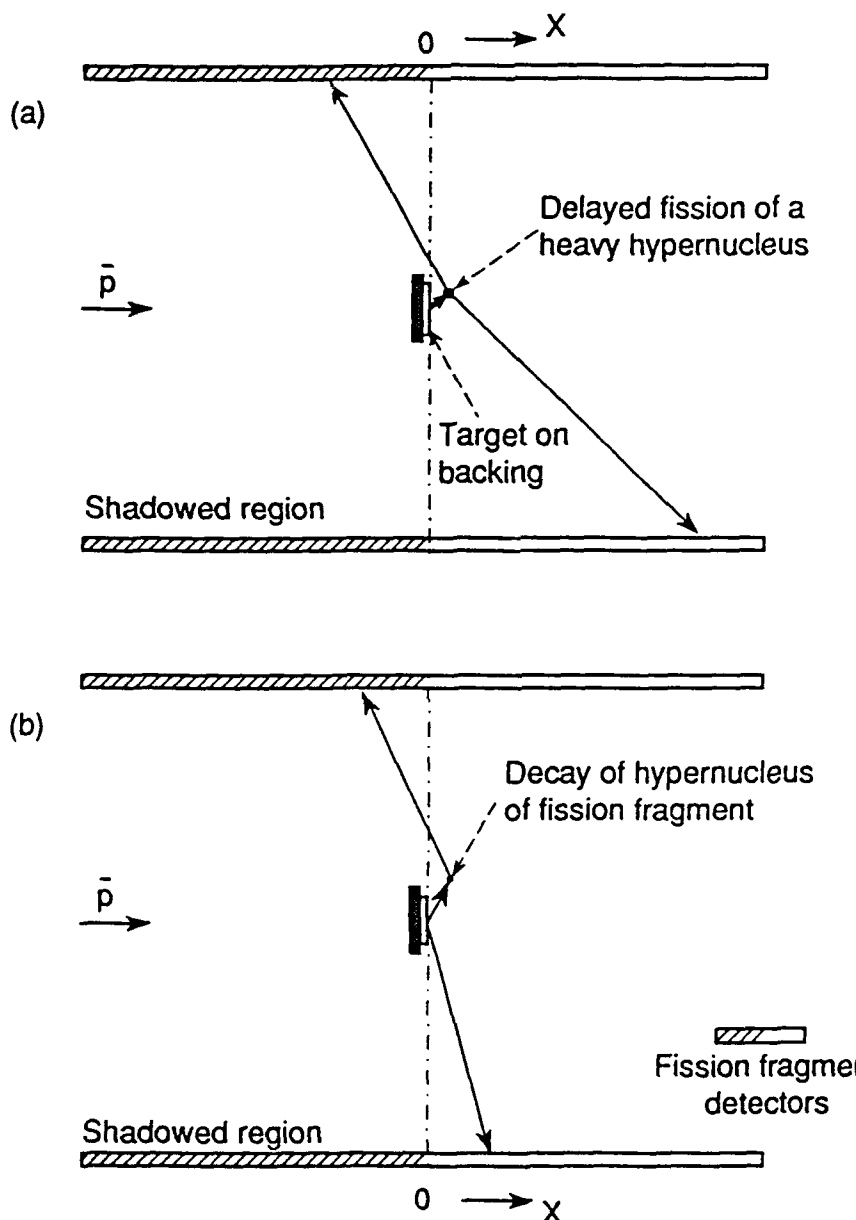


Figure 1

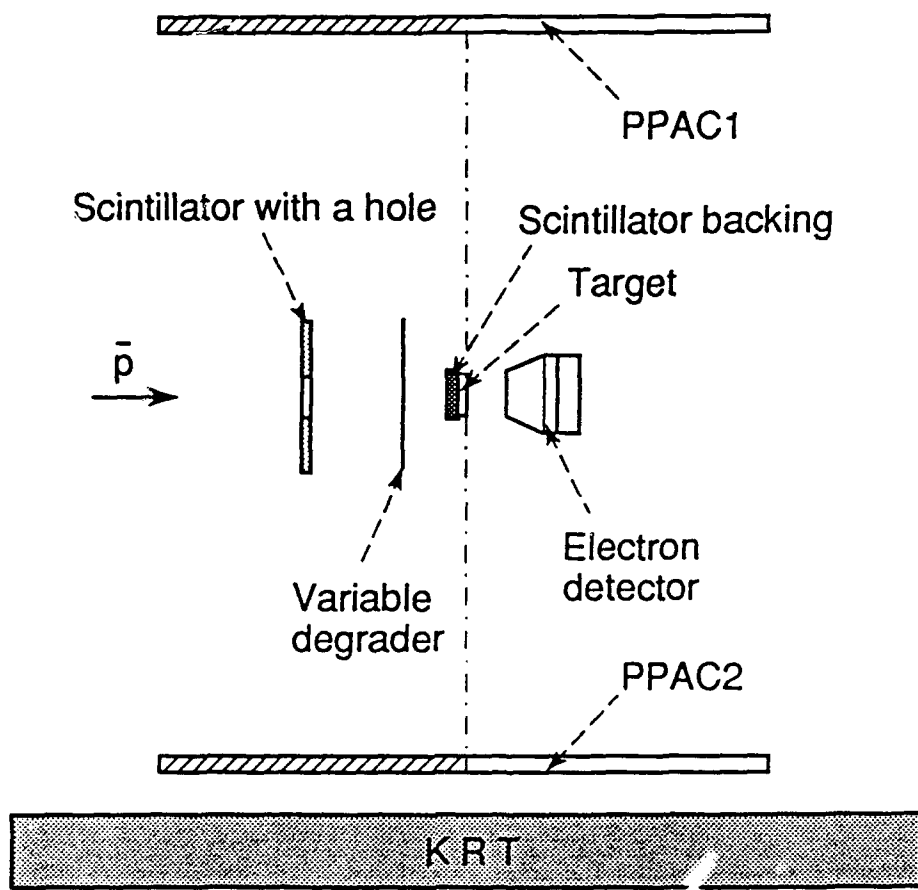


Figure 2

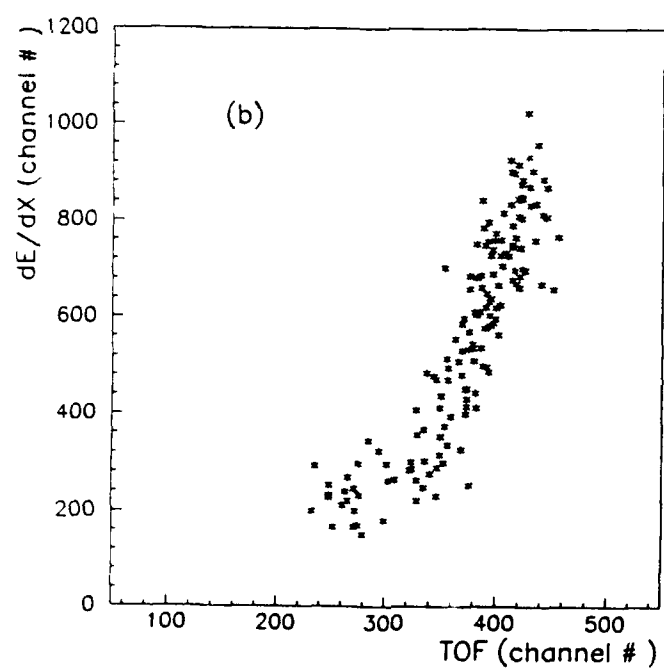
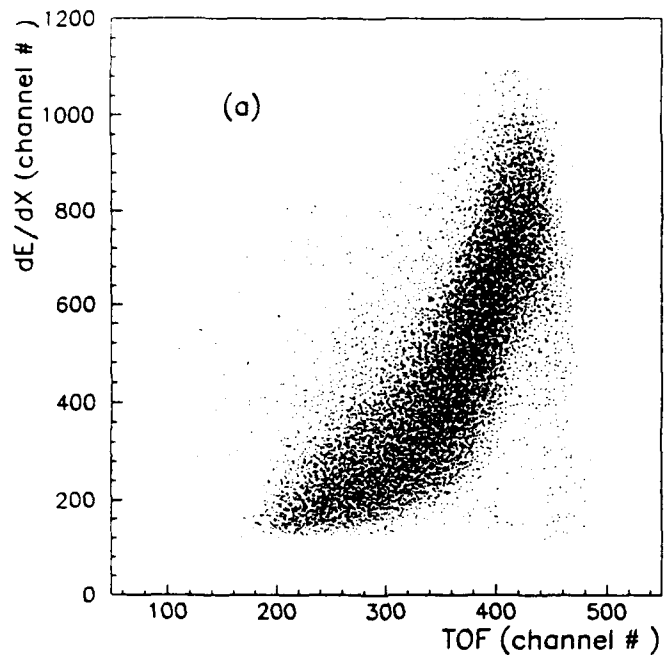


Figure 3

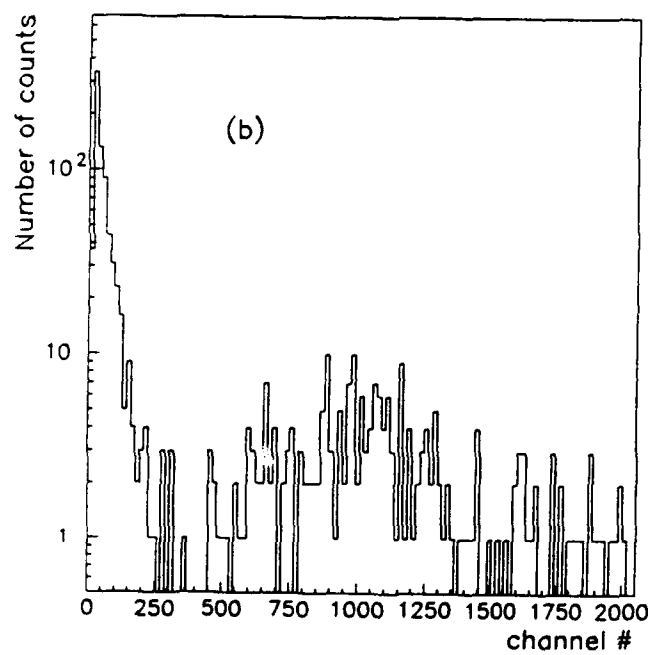
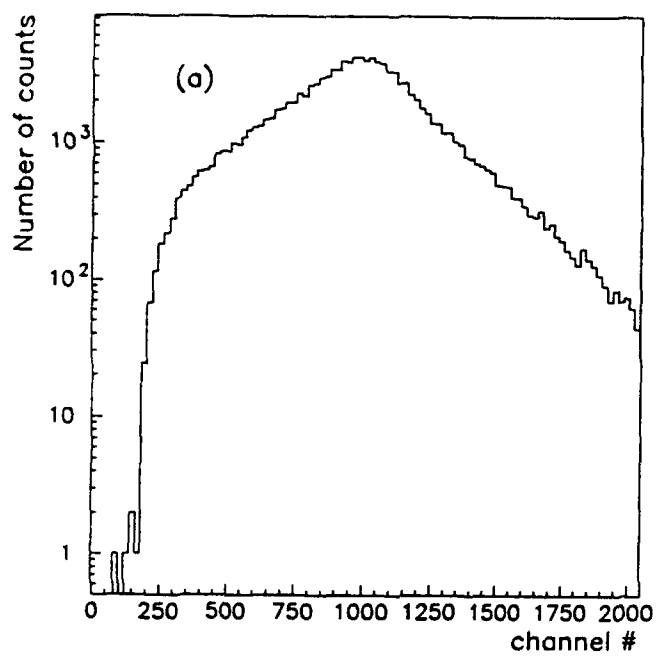


Figure 4

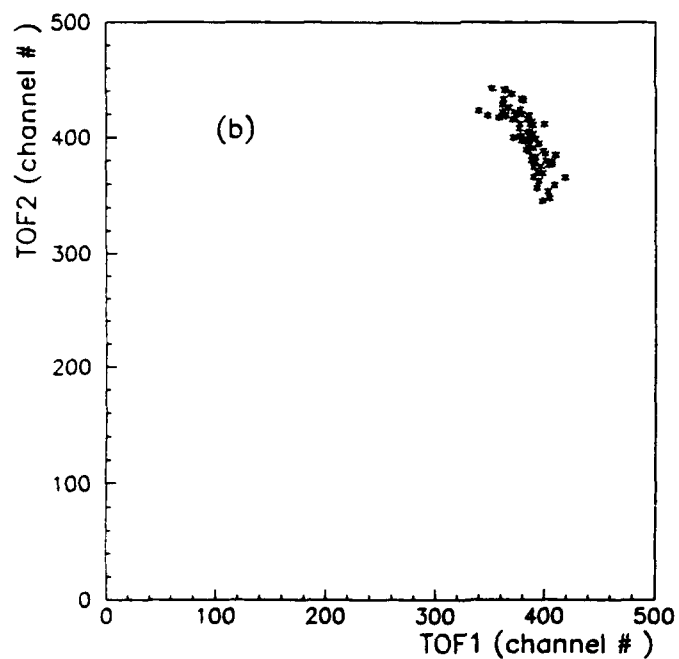
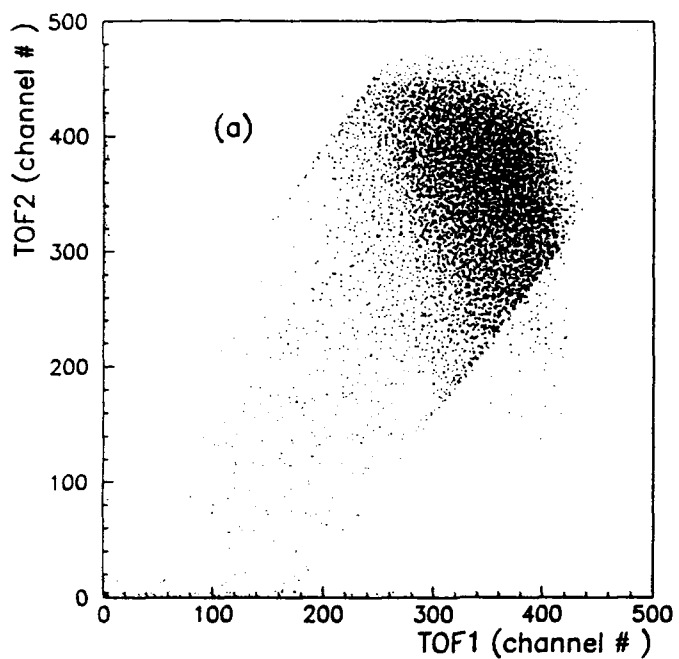


Figure 5

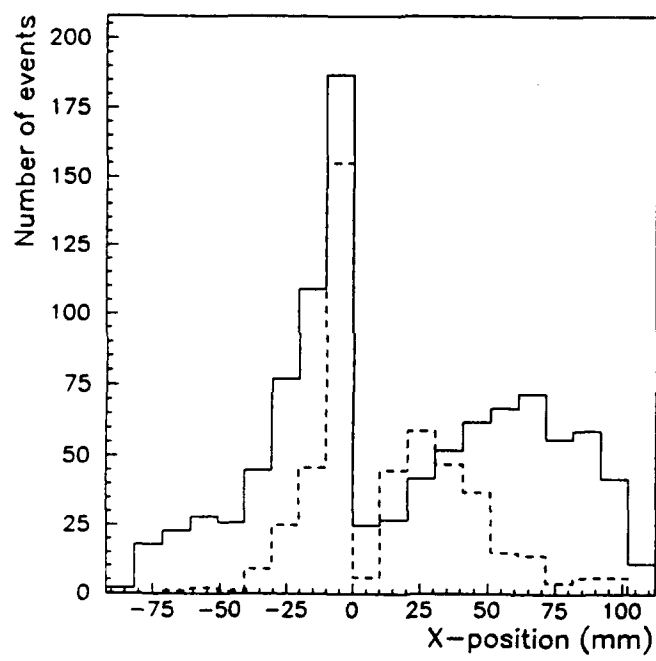


Figure 6

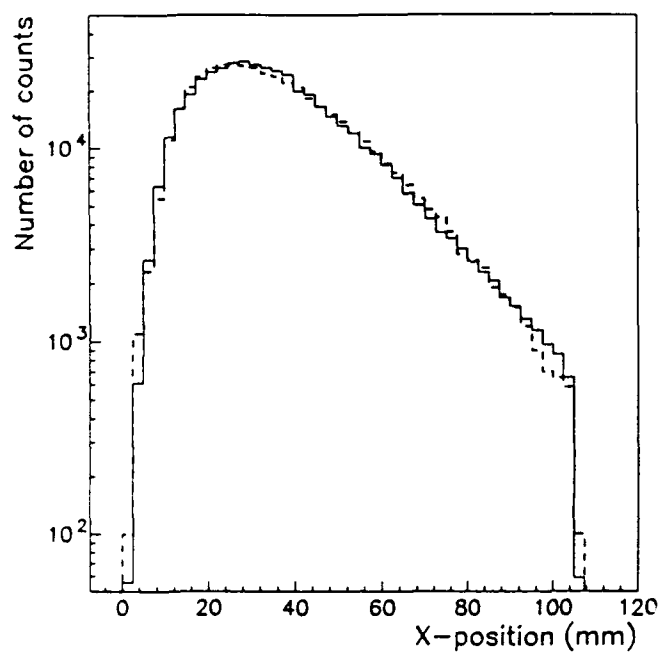


Figure 7

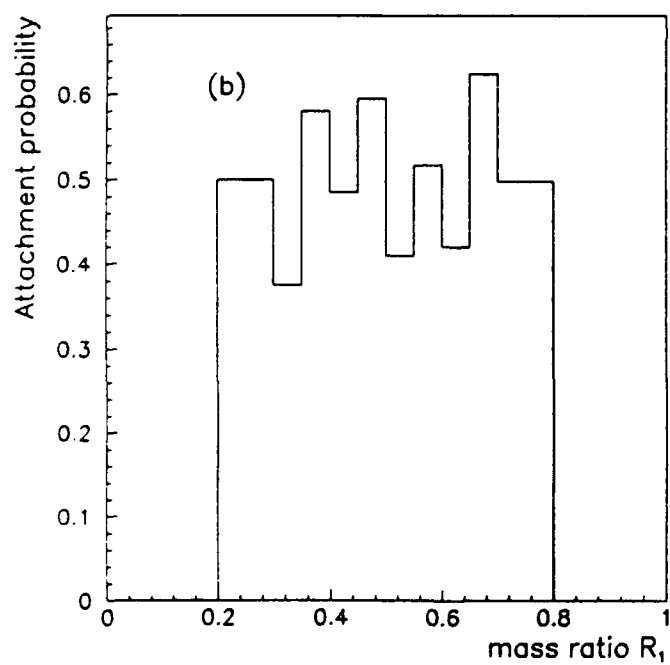
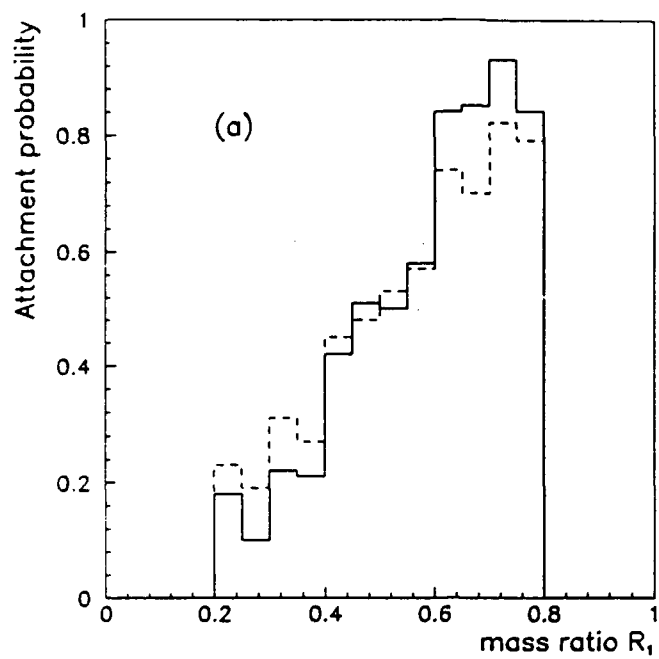


Figure 8

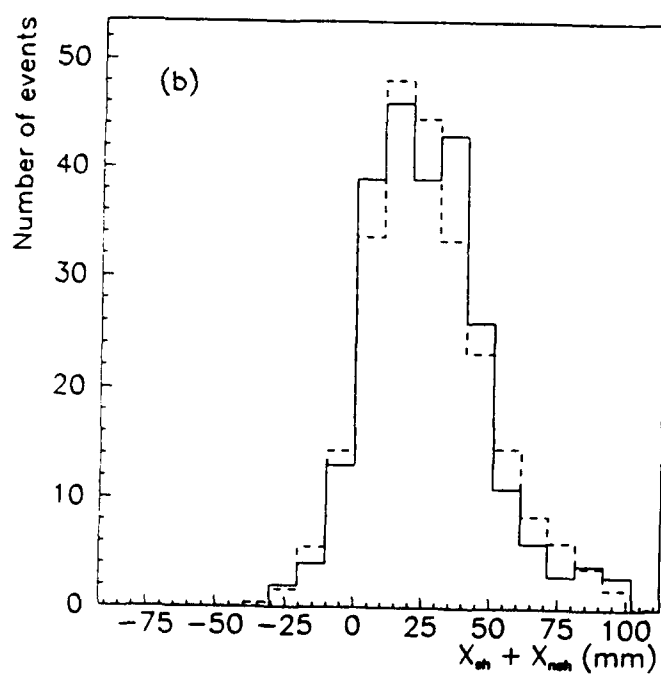
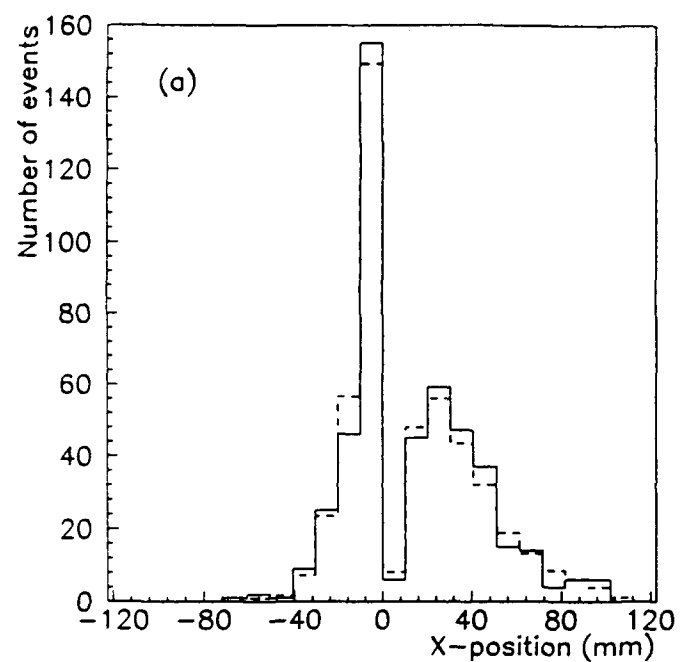


Figure 9

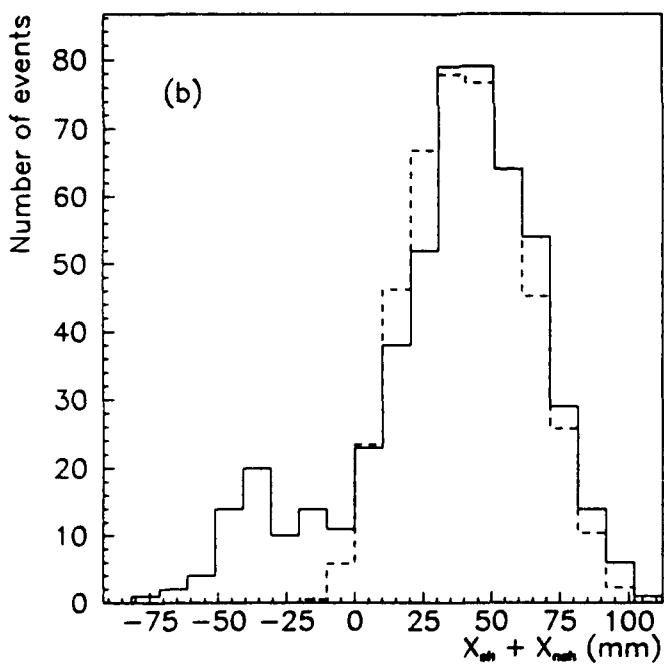
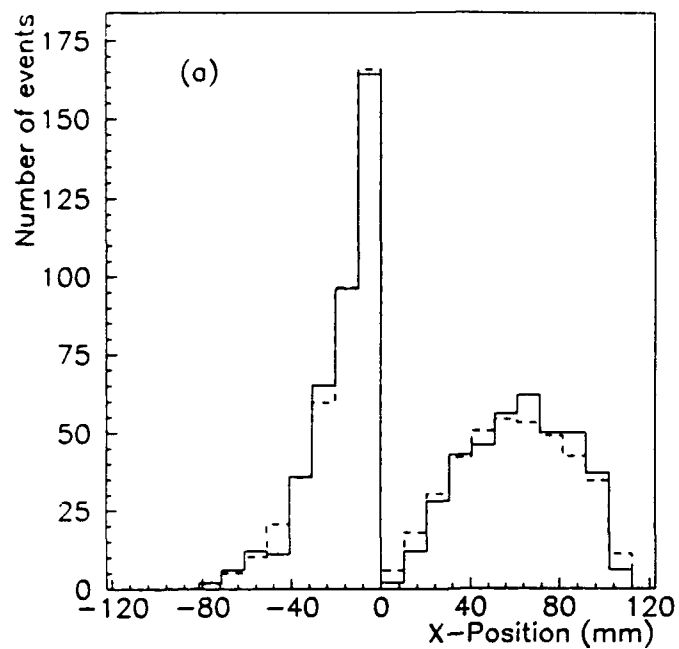


Figure 10

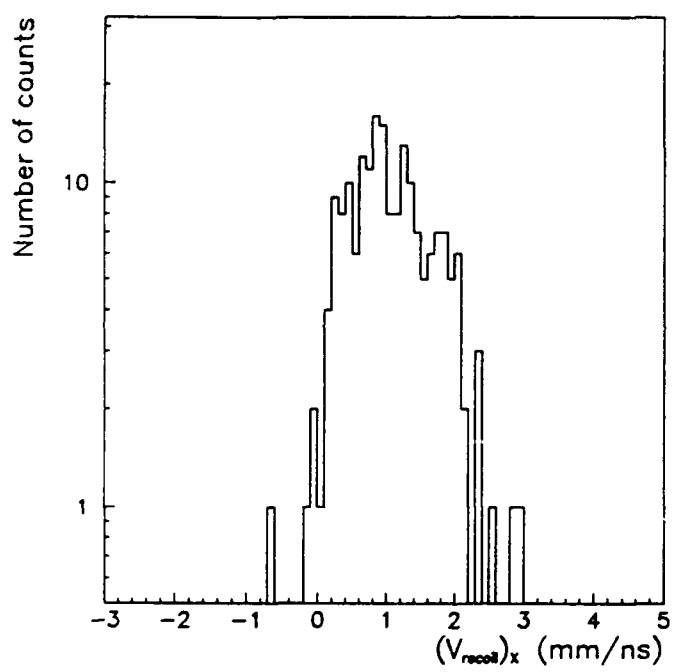


Figure 11

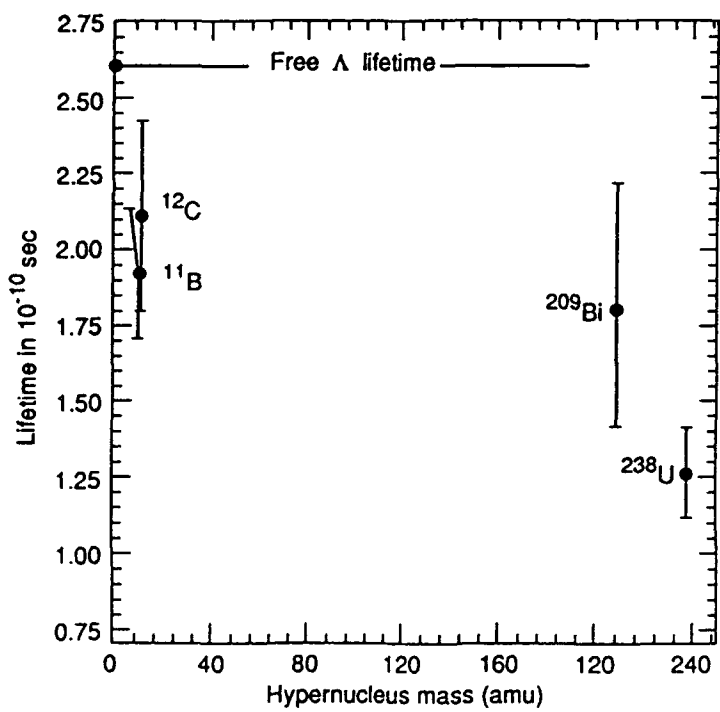


Figure 12